Progress in Oceanography 229 (2024) 103373

Contents lists available at ScienceDirect

Progress in Oceanography

journal homepage: www.elsevier.com/locate/pocean

Perspectives on Northern Gulf of Alaska salinity field structure, freshwater pathways, and controlling mechanisms

Isaac Reister *, Seth Danielson, Ana Aguilar-Islas

College of Fisheries and Ocean Sciences, University of Alaska Fairbanks, Fairbanks, AK 99775, USA

ARTICLE INFO

Keywords:
River plumes
Freshwater
Entrainment
Satellite remote sensing
Self-organized mapping
Surface ekman layer
Aleutian low wind
USA, Alaska, Northern Gulf of Alaska
USA, Alaska, Copper River

ABSTRACT

The biologically productive Northern Gulf of Alaska (NGA) continental shelf receives large inputs of freshwater from surrounding glaciated and non-glaciated watersheds, and a better characterization of the regional salinity spatiotemporal variability is important for understanding its fate and ecological roles. We here assess synoptic to seasonal distributions of freshwater pathways of the Copper River discharge plume and the greater NGA continental shelf and slope using observations from ship-based and towed undulating conductivity-temperature-depth (CTD) instruments, satellite imagery, and satellite-tracked drifters. On the NGA continental shelf and slope we find low salinities not only nearshore but also 100–150 km from the coast (i.e. average 0–50 m salinities less than 31.9, 31.3, and 30.8 in spring, summer, and fall respectively) indicating recurring mid-shelf and shelf-break freshwater pathways. Close to the Copper River, the shelf bathymetry decouples the spreading river plume from the direct effects of seafloor-induced steering and mixing, allowing iron- and silicic acid-rich river outflow to propagate offshore within a surface-trapped plume. Self-organized mapping analysis applied to true color satellite imagery reveals common patterns of the turbid river plume. We show that the Copper River plume is sensitive to local wind forcing and exerts control over water column stratification up to ~100 km from the river mouth. Upwelling-favorable wind stress modifies plume entrainment and density anomalies and plume width. Baroclinic transport of surface waters west of the river mouth closely follow the influence of alongshore wind stress, while baroclinic transport east of the river mouth is additionally modified by a recurring or persistent gyre. Our results provide context for considering the oceanic fate of terrestrial discharges in the Gulf of Alaska.

1. Introduction

The northern Gulf of Alaska (NGA; 140° and 155° W and between 57° N and the Alaskan mainland) is surrounded by steep glaciated and nonglaciated terrain that outputs large quantities of freshwater into the marine environment. Salinity organizes the NGA water column density and mediates nutrient fluxes into the euphotic zone (Whitney et al., 2005) in this productive ecosystem, which sustains commercial, recreational, and subsistence fish harvests important for the socioeconomic well-being of coastal Alaskan communities (Himes-Cornell & Kasperski, 2016; McDowell Group, 2020; Sumaila et al., 2011). In this study, we examine the NGA hydrographic structure with particular focus on spatial and temporal salinity variability as resolved by spring, summer, and fall shipboard surveys. The *in situ* data depict seasonally varying pan-NGA salinity distributions and pathways, allowing us to examine factors that control the fate of riverine freshwater entering the marine environment and its spatial and temporal structure. Twenty-five years of data collected along a repeat cross-shelf transect contribute to analysis of low salinity anomalies at key monitoring stations, while recent shipboard surveys provide along-shelf context, including from high resolution CTD surveys in the vicinity of the Copper River (CR) discharge plume.

Salinity is the main driver of seawater density over most of the water column in the NGA and other high latitude oceans, while temperature is often a secondary controller (Carmack, 2007). Variations of NGA salinity over the continental shelf derive in part from a massive annual fresh water discharge from land, estimated at ~ 725 km^3y^{-1} (Royer, 1982) for the coast of Alaska between 130° W to 150° W. Subsequent studies for similar spatial extents have estimated terrestrial runoff to be in the range of 728–870 km^3y^{-1} (Wang, 2004; Neal et al., 2010; Hill et al., 2015; Beamer et al., 2016). If we restrict our consideration to the NGA bounded by 140° W to 155° W and north of 57° N to the coast,

Abbreviations: NGA, Northern Gulf of Alaska; FWH, Freshwater height.

* Corresponding author.
E-mail address: isaac.reister@gmail.com (I. Reister).

https://doi.org/10.1016/j.pocean.2024.103373
Received 26 April 2024; Received in revised form 18 October 2024; Accepted 29 October 2024
Available online 8 November 2024

annual freshwater output is ~ 249 km^3y^{-1} (Beamer et al., 2016) with the CR in south central Alaska (Fig. 1) accounting for over one fifth of this total. We here examine linkages between the CR discharge plume and the greater NGA, as well as the sensitivity of the plume to discharge rate and wind direction within 50 km of the river delta.

1.1. Oceanographic setting

Oceanic hydrographic and flow field structure of the NGA is shaped by frequent North Pacific storms associated with the Aleutian Low sea level pressure cell (Rodionov et al., 2007). These storms drive downwelling-favorable cyclonic winds in the NGA for much of the year and help maintain a coastally trapped "wedge" of low salinity waters that characterizes the NGA coastal region (Livingstone and Royer, 1980). However, solar heating, reduced downwelling and even weak but persistent upwelling conditions during summer months help maintain a relatively shallow surface mixed layer and potential for offshore-directed near-surface flows (Livingstone & Royer, 1980; Stabeno et al., 2004; Williams et al., 2007). Wind orientation along the NGA coast is primarily bimodal and aligned parallel to the coast; alongshore winds near the coast can be strengthened by barrier jets (Loescher et al., 2006).

Coastal runoff also contributes to the seasonal density structure, which for some purposes can be approximated as a two-layer system divided at ~100 m (Royer, 2005). Minimum upper layer salinities occur in October and maximum lower layer salinities in August (Childers et al., 2005; Royer, 2005). The lower layer responds as downwelling relaxes throughout summer months, causing near-seafloor and interior flows to compensate the offshore surface transport by drawing high salinity water from the outer shelf (Weingartner et al., 2005). In the summer upper layer, coastal freshwater discharge spreads cross-shelf during weak and upwelling-favorable wind conditions, but downwelling winds and geostrophy attempt to counteract the spreading tendency. As the dominant density control over most of the water column, salinity generally increases with depth in all seasons. Shelf-wide hydrographic structure begins to reset in fall, when winds increase, downwelling strengthens, ocean–atmosphere heat fluxes switch from oceanic heat gain to heat loss, and coastal freshwater discharge declines as precipitation begins to fall as snow at high elevations while the rate of low elevation snowpack melt declines.

The NGA hydrography as a whole and the Alaska Coastal Current (ACC) in particular are driven and structured by downwelling-favorable winds, freshwater runoff, and the underlying seafloor topography. The

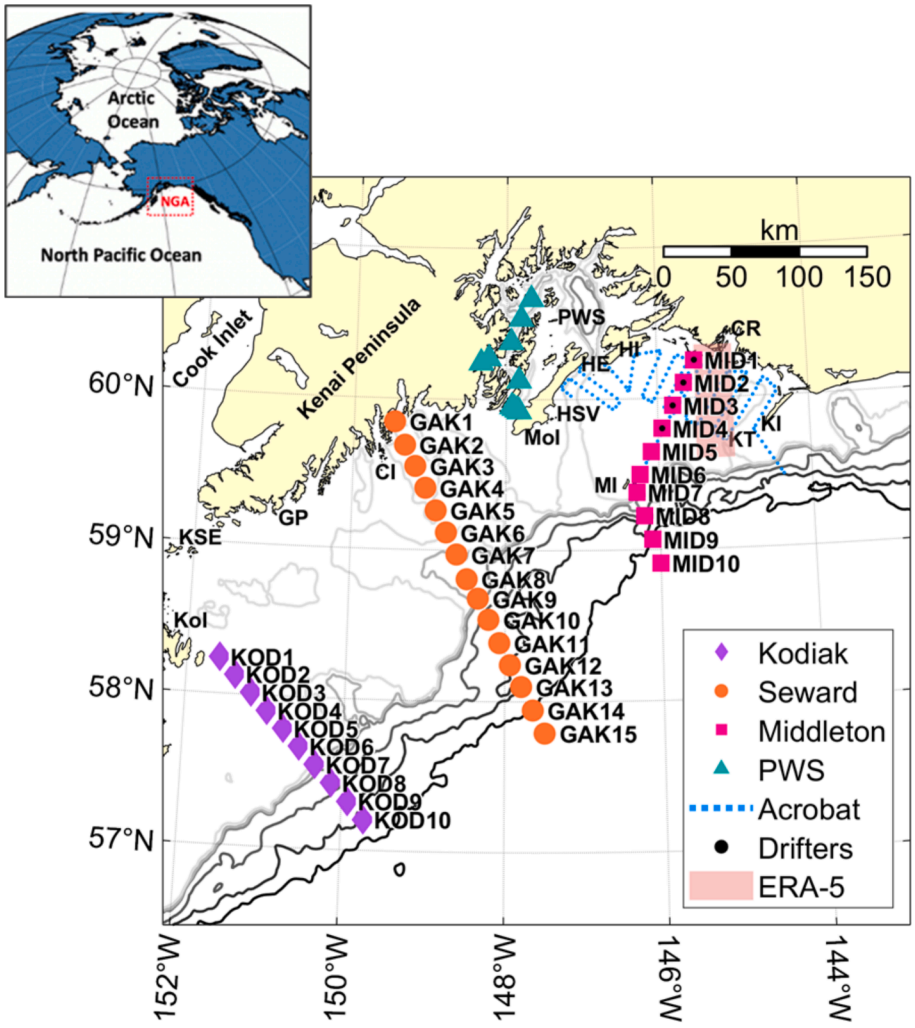

Fig. 1. Locations of stations for the Kodiak (KOD), Seward (GAK), Middleton (MID) and Prince William Sound (PWS) sampling stations. Kodiak and Middleton Lines were surveyed 2018–2021. The Seward Line was surveyed 1997–2021. The upshelf direction is nominally eastward; downshelf is to the west. Also shown are the cruise track for the July 2020 Acrobat tow, July 2019 drifter deployment locations, and the ERA-5 wind reanalysis bounding box. Place name abbreviations include Copper River (CR), Kayak Island (KI), Kayak Trough (KT), Middleton Island (MI), Hinchinbrook Island (HI), Hinchinbrook Sea Valley (HSV), Montague Island (MoI), Chiswell Islands (CI), Gore Point (GP), Kennedy-Stevenson Entrance (KSE), and the western tip of Kodiak Island (KoI). Bathymetry contours from light grey to black delineate 175, 250, 325, 1000, 2000, and 3000 m depths.

ACC buoyant coastal current is typically confined within ~ 50 km of the coast and comprised of lower salinity water than that found farther offshore (Royer, 1982; Weingartner et al., 2005). Baroclinic flow is maintained by the horizontal density front and onshore Ekman transport, carrying an annual mean of ~ 2.8×10^4 m^3 s^{-1} of freshwater westward along the Kenai Peninsula, some of which is lost offshore via eddy fluxes (Weingartner et al., 2005). Topographic steering at sharp promontories like Kayak Island (Fig. 1), the Chiswell Islands, and Montague Island are thought to occasionally divert low salinity ACC water away from the coast and onto the mid and outer shelf (Klinger, 1994; Stabeno et al., 2016). Satellite-tracked drifters deployed over the continental shelf upstream of Kayak Island suggest that ACC waters can be diverted along the continental slope near Kayak Island, indicating a splitting, redirection, or at least temporary interruption to the coastally confined ACC flow (Stabeno et al., 2016). The ACC continues or re-forms northwest of Kayak Island (Stabeno et al., 2016), fed by the CR outflow and other smaller river inputs. Alongshore winds and freshwater input control the baroclinic transport of the ACC (Weingartner et al., 2005; Stabeno et al., 2016), which is sensitive to temporal and spatial variability in either control. The relative contribution of each driver to the baroclinic transport is in part a function of local setting. For example, alongshore wind contributes more to baroclinic transport at Gore Point (Stabeno et al., 2016) than at the Seward Line (Fig. 1) where freshwater discharge is an important factor (Weingartner et al., 2005), because the inner shelf region of the Seward Line is closer to large sources of coastal freshwater runoff such as the outflow from Prince William Sound (PWS) and the CR.

As it circumscribes the NGA, ACC continuity can be interrupted by gap winds, upwelling-favorable winds, and topographic steering, all of which can detach low salinity ACC water from the coast. Gap winds at Kennedy-Stevenson Entrance (Fig. 1) cause occasional locally offshore-directed currents, but such winds are thought to have little influence on the ACC near the Seward Line (Ladd et al., 2016). Gap winds also occur in the CR delta (Loescher et al., 2006; Macklin et al., 1988) and may modify low salinity plumes there. Due to the geometry of cyclonic wind systems, upwelling-favorable winds are more likely to occur in the western NGA than in the east, where storms tend to stall and dissipate (Mesquita et al., 2010; Stabeno et al., 2004). If upwelling-favorable winds are sufficiently sustained (e.g., more than one or two inertial periods) they can drive an Ekman transport response, advecting low salinity water away from the coast (Fong & Geyer, 2001; Williams et al., 2007).

1.2. The Copper River

Numerous glaciers feed the CR, which discharges ~ 51 km^3 $year^{-1}$ of freshwater and ~ 63×10^6 tonnes $year^{-1}$ of suspended sediment (Brabets, 1997). This sediment load is similar to that of the Yukon River, which has an average annual volume discharge about four times that of the CR (Brabets, 1997). Sediments are visible in true-color satellite imagery and have been used as coastal water tracers both near the CR (Ahlnäs et al., 1987) and in other rivers with high sediment loads, such as the Mississippi River (Salisbury et al., 2004; Walker, 1996; Walker et al., 2005) and the Fraser River (Pawlowicz et al., 2017).

The CR outflow encounters a relatively short estuarine mixing zone (Brabets, 1997) and the subsequent effects of this geomorphology helps structure the character of its plume farther offshore. The CR delta, comprised of shallow (< 2 m) tidal mudflats inside a series of barrier islands, spans an area of approximately 500 km^2 but extends only 10 km cross-shore (Powers et al., 2002). Many other regions of freshwater influence (ROFIs), such as the low salinity plumes that advect from Chesapeake Bay and the conglomeration of bays at the Hudson River mouth, have more extensive mixing zones (Choi & Wilkin, 2007; Lentz, 2004; Rennie et al., 1999), allowing these other discharges greater opportunity to blend with shelf waters. With a short mixing zone we expect the CR plume to have buoyancy gradients that make it particularly susceptible to wind stress forcing (Lentz, 2004). Under sustained upwelling-favorable winds, highly buoyant plumes not only advect offshore (Fong & Geyer, 2001) but may also extend upshelf under sufficient forcing (Houghton et al., 2004; Kourafalou et al., 1996). The shelf orientation is defined by the Kelvin wave propagation direction (coast to the right for downshelf progression in the Northern Hemisphere), so the upshelf direction is nominally eastward along the Copper River and NGA coastlines.

A 3D ocean circulation model hindcast integration suggests that the CR plume generally follows the course of the ACC (Wang et al., 2014). In the model, variability in a passive tracer defines the CR plume's spatial and temporal evolution and reflects a balance between freshwater discharge buoyancy and wind stress. The modeled plume develops as a surface-trapped feature with a mean depth of ~ 10 m, although contrasting seasonal wind patterns result in similarly contrasting plume characteristics. Downwelling-favorable winds constrain the plume within 25 km of the coast, while calm winds lead to the development of a larger bulge with a 60 km cross-shelf extent (Wang et al., 2014). The Wang et al. (2014) results are in accordance with an Ekman driven downwelling response (Moffat & Lentz, 2012) and bulge development (Kourafalou et al., 1996). When exiting the CR region, about two-thirds of the water coming from the CR moves westward past Montague Island, bypassing PWS; one-third enters the Sound before eventually exiting back to the shelf via Montague Strait; and a small fraction is lost to the cross-shelf direction (Wang et al., 2014). Jaeger et al. (1998) inferred similar flow pathways from the secondary deposits of CR sediments along Kayak Trough, Hinchinbrook Sea Valley, and the eastern entrances of PWS.

1.3. Approach

The work presented herein is part of the Northern Gulf of Alaska Long Term Ecological Research (NGA LTER) site, which supports an interdisciplinary effort to better understand the ecological functioning of the NGA marine system, including the importance of resilience in setting key NGA emergent ecological properties via physical and chemical dynamics, carbon cycling, biological community structure and species interactions (Hopcroft et al., 2016). Here ecological resilience is defined as the maintenance of ecosystem function following disturbance (Holling, 1973; Levin & Lubchenco, 2008). For example, coastal runoff increases the nearshore water column stability in the NGA (Henson, 2007), which helps mediate the vertical distribution of nutrients. The ecological properties in the context of freshwater pathways include those influencing the CR plume: wind forcing, stratification, and entrainment all likely play important ecological roles through their influence on nutrient supply (Lohan & Bruland, 2006), phytoplankton growth (Lohrenz et al., 1999), and light availability and grazing (Harrison et al., 1991). Nitrate and iron have a riverine source and often function as limiting nutrients that influence phytoplankton community structure in the NGA (e.g., Aguilar-Islas et al., 2016; Strom et al., 2006). The CR is also a source of other nutrients including silicic acid (Brown et al., 2010).

This study is focused on better revealing the regional physical structure of the NGA and factors that mediate the advection and mixing of low salinities in the upper water column (<50 m). We investigate locations of recurring low salinity sites along the Seward Line, and the physical dynamics of the Copper River plume driven by wind and river discharge. Previous studies have concentrated on the ACC, with a focus on mass transport parameters, physical drivers, and continuity (e.g. Stabeno et al., 2016; Weingartner et al., 2005; Ladd et al., 2016), while the Copper River plume has mostly been examined through a single two-year model simulation validated by CTD profiles (Wang et al., 2014). Using *in situ* data we provide evidence of freshwater pathways beyond the ACC out to the slope, and we assess drivers that contribute to these freshwater pathways. We study interactions between freshwater discharge, wind and hydrographic structure using ship-based

hydrography, towed undulating CTD instruments, satellite imagery, satellite-tracked drifters, river discharge data, and atmospheric reanalysis products.

Section 2 of this paper describes the data and data handling methods; Section 3 presents our results for freshwater pathways across the NGA and within the CR region; Section 4 provides discussion of results and a summary.

2. DATA and methods

2.1. Shipboard Hydrography

NGA LTER sampling transects consist of the Seward Line (GAK stations), the Middleton Line (MID stations), the Kodiak Line (KOD stations), and stations in PWS (Fig. 1). Seward Line hydrographic data were collected 2–7 times per year from 1997 to 2021. These one- to three-week research cruises typically consist of 40–80 sampling stations that include up to 15 core Seward Line stations and stations within PWS; sampling on the Middleton Island and Kodiak Island transects began in 2018. From 2018 to 2021 NGA LTER cruises were conducted in April-May, July and September, corresponding to mid-spring, mid-summer and early-fall. Shelf stations are spaced 15–17 km apart. Inclement weather occasionally inhibits sampling, during which times the Seward Line station set is prioritized (Table 1).

Temperature and conductivity data were logged with a SBE9/11 system (24 Hz sample rate) outfitted with dual SBE 3plus and SBE 4 probes, respectively. Conductivity-temperature-depth (CTD) data were processed in the SBE Data Processing scripting and computational toolbox (Sea-Bird Scientific, 2017) and then edited using custom MATLAB software for removing data spikes associated with surface bubbles, planktonic biofouling of the conductivity cell and other obvious outliers. Data deemed erroneous were replaced with values obtained by linearly interpolating between adjacent good data, or if in the upper few meters of the water column, extrapolating the shallowest good data point to the sea surface.

Freshwater height (FWH) for the upper 50 m of the water column was calculated using the difference between the *in situ* salinity and a reference value (S_r = 33.8), which represents the base of the NGA's permanent halocline (Dodimead et al., 1963; Musgrave et al., 1992). The FWH relation is:

$$\mathrm{FWH} = ((S_r{}^*\rho_r{}^*d)/S_s{}^*\rho_s) - d \quad (1)$$

where S is practical salinity, ρ is density, subscripts r and s designate reference and station, respectively, and d is the integration depth. S_s is calculated as the average practical salinity between the surface and depth d. For the few stations with water depth < 50 m (~0.05 % of stations), the deepest depth available was used. Results presented here are insensitive to other integration depths (e.g., 75 m and 100 m). FWH was calculated for the Middleton and Kodiak lines from 2018 to 2021. FWH along the Seward Line was calculated for 59 Seward Line CTD transects (1997–2021) across stations GAK1 through GAK13. The data were subset into spring (April 19 – May 27), summer (June 30 – July 24), and fall (September 1 – October 14), see Table 1 for the distribution between these months.

A bootstrap analysis was applied to the Seward Line salinity data (59 cruises from 1997 to 2021; Table 1) to assess the structure of cross-shelf salinity gradients, which may be less susceptible than salinity to inter-annual variation in freshwater output from the coast (Thomson & Emery, 2014b). The data were subset into the same date limits as the FWH analysis, and salinity was averaged at each station across the 0–100 m depth interval prior to sequentially applying forward derivatives, starting with the nearshore station. Significant differences between adjacent salinity gradients were ascribed when 95 % confidence intervals for bootstrapped distributions of the differences between adjacent-station-set salinity gradients did not contain zero (Greenland et al., 2016). Bootstrap analyses were run 10,000 times to generate normalized distributions. Standard statistical metrics of mean (μ), standard deviation (σ), Pearson's correlation (r) and p-values are used herein to quantitatively summarize and assess our findings.

Table 1
Number of occupations per month (April to October) for the entire study duration for the Seward Line (1997–2021), Middleton and Kodiak Lines (2018–2021) and Prince William Sound (2018–2021).

Month	Number of Occupations Seward Line	Number of Occupations Middleton Line	Number of Occupations Kodiak Line	Number of Occupations Prince William Sound
April	1	3	2	3
May	24	0	1	1
June	1	0	0	2
July	8	4	3	2
August*	0	0	0	0
Sept.	17	3	2	4
Oct.	8	0	0	0

* No sampling occurred during August.

2.2. Towed CTD

We towed an Ocean Sciences Inc. Acrobat® undulating vehicle across the CR region over 4–8 July 2019, 27 July 2019, and 11–14 July 2020. The instrument sampled to a maximum depth of 65 m and minimum depth of 1 m, moving with a vertical speed of approximately 1 m/s. It was towed ~ 200 m astern of the ship, which traveled at 3–3.5- m/s through the water. The Acrobat was equipped with a SBE 49 FastCat CTD sampling at 16 Hz and positional information came from the shipboard GPS system logged at 1 Hz.

Using in-house MATLAB scripts (Martini et al., 2023), the Acrobat CTD data was initially gridded to 0.5 dbar bins vertically and corrected for thermistor thermal response, time lag due to the physical separation of the temperature and conductivity sensors, and conductivity sensor thermal lag following Johnson et al. (2007). Changes in the temporal gradient of pressure were used to identify turning points in the towed data. Pairs of upcasts and downcasts connected by a surface turning point were averaged to form a single vertical profile and assigned a position that matched the surface turning point coordinates. Surface turning points occurred along the transects typically every 0.5 km. The GPS and CTD were merged into two datasets that were horizontally gridded with 1 km and 5 km bins.

Additional in-house MATLAB scripts were used for final quality control and missing data interpolations (commonly needed near the surface). Corrections included the following: removal of casts that either don't reach 33 m depth in deep water or 50 % of the target depth range in shallow water; filling missing surface (< 10 m depth) data; and additional interpolations. Final data was then binned to 1 dbar levels down to 65 dbar.

The 4–8 July 2019 and 11–14 July 2020 Acrobat datasets had similar spatial coverage and were used to compare the inner shelf hydrographic structure of those two years. To facilitate the comparison, the two datasets were spatially interpolated onto a 2.3 km by 2.7 km 3D grid bounded by 59.2 to 60.4 °N and 147.6 to 143.5 °W, and across 0 to 45 dbar in 1 dbar increments. Transects were defined that started at the nearshore grid points where the two datasets overlapped and extended 35 km offshore following the orientation of the 2020 cross-shore cruise tracks (Fig. 1).

Baroclinic geostrophic velocities for Acrobat CTD datasets were based on the thermal wind relation with an assumed level of no motion at H = 45 dbar (the deepest depth consistently shared by July 4–8, 2019 and July 11–14, 2020 surveys). Reference levels for nearshore bottom depths shallower than the level of no motion used the deepest common depth between each adjacent station pair. The reference velocity for the

shallower station pair was then obtained from the next-adjacent offshore (deeper) velocity profile (Helland-Hansen, 1934). Reference velocities are approximated as the alongshore baroclinic geostrophic current derived from the geopotential anomaly along a transect of practical salinity and temperature. The alongshore baroclinic component of the mass transport (M_{bc}) is:

$$M_{bc} = \int_0^{L_y} \int_{-H}^{0} U_{bc}(y,z)dzdy \quad (2)$$

For the interpolated Acrobat data, the length of cross-shore transect L_y = 35 km, H = 45 m, and $U_{bc}(y,z)$ is the alongshore baroclinic geostrophic current component at depth z and offshore distance y. For other applications of Equation (2) H is specified in the results.

For computing alongshore near-surface baroclinic geostrophic currents, the reference level for the Acrobat data was limited to 45 dbar due to the profiling range of the instrument. Current velocity data from a Teledyne RDI Workhorse Sentinel 300 kHz acoustic Doppler current profiler (ADCP) were collected in July 2019, 2020, 2022, and 2023. These data were acquired with the University of Hawaii Data Acquisition System (UHDAS) and post-processed with the Common Ocean Data Access System (CODAS) (Firing et al., 2012). Strong tides on the NGA shelf preclude applying ship-measured ocean currents to form uncontaminated subtidal absolute geostrophic velocity estimates, but the velocity data do allow us to compare the instantaneous flow field speeds with the computed baroclinic current magnitudes. After rotating the dataset, average alongshore (u_c) and cross-shore (v_c) components from 50-75 m were obtained along the 2020 Acrobat grid pattern (Fig. 1). The mean u_c for all data combined (615 sample points) was -0.02 ± 0.09 m/s and the mean v_c was -0.01 ± 0.13 m/s where negative values respectively indicate downshelf and onshore directions. The absolute value of the mean ADCP current velocities plus the standard deviation are about a quarter of the magnitude of the CR plume's alongshore baroclinic jet (~0.3-.4 m/s).

2.3. Coastal discharge data

The USGS Million Dollar bridge streamflow gauge (station 15214000) provided CR discharge data from 2005 to 2021, except for 2008 when it was out-of-service. The gauge is located at the outflow of Miles Lake, ~45 km inland of delta's tidal mudflats and at an elevation of 38 m above sea level. The gauge station consistently logged data from May to September but often became inoperable in other months due to ice and equipment malfunction (Conaway, pers. comm.). May to September discharge data was recorded at 15-minute intervals. We averaged the raw data by hour and day; a seasonal median was also computed from monthly averages of the discharge data (Fig. 2). A specific comparison of the plume response to wind direction was made under high discharge conditions, which were determined by limiting the discharge data to values above two-thirds of the seasonal median in July. From Brabets (1997) assessments of river areal cross-sections and flow rates, we estimate a time lag of 31–44 h for water to transit between the Million Dollar bridge and the CR delta barrier islands from May to September; (see supplementary text for more details). Based on those estimates we applied a 38-hour lag to the river discharge dataset, then constructed 24-hour daily river discharge averages beginning at 13:00 UTC to match satellite imagery with coincident river discharge conditions.

2.4. Wind data

We use the European Climate Model Weather Forecast (ECMWF) reanalysis version 5 (ERA-5) (Hersbach et al., 2020) for estimates of hourly eastward and northward 10 m wind velocity components (u and v, respectively) for 2002–2021. ERA-5 is computed at a spatial resolution of 0.25°. From 12 model grid points just south of the CR delta we

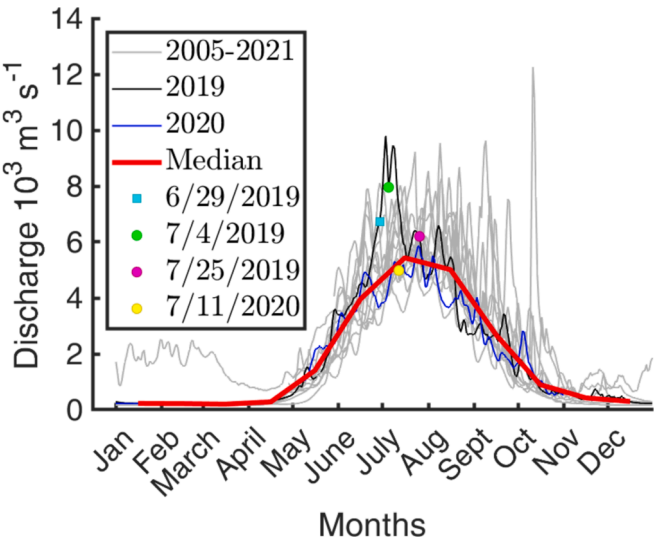

Fig. 2. Fresh water discharge recorded at the Copper River's Million Dollar bridge. Thin lines show daily average discharge for 2005–2021 (gray), 2019 (black), and 2020 (blue); the thick red line is the median of the monthly averages from all years. Colored markers indicate the Acrobat transects across stations MID1-MID6 (circles) and satellite image (cyan square).

formed a 2290 km^2 spatial average centered at 59.975 °N, 145.250 °W (Fig. 1). Principal component analysis determined that the highest variance in wind velocity is nominally alongshore, oriented at an angle of 18.5° clockwise from east. M_{bc} is controlled by density gradients, which in turn are shaped by wind driven Ekman dynamics; we anticipate a time lag between wind changes and the M_{bc} response. By assessing a range of lags (0–30 h) and smoothing via a moving mean window (range 1–50 h) we found that the strongest correspondence (r^2 = 0.47) coincided with a lag of 12 h (local inertial period = 14 h) and a 13-hour centered moving mean window. To match satellite imagery with coincident wind conditions, 24-hour daily wind vector averages beginning at 13:00 UTC were constructed using the same grid points.

2.5. Satellite tracked drifter data

One Pacific Gyre Microstar and two Oceanetic Measurement SCT drifters were deployed during the July 2019 process study at each of the four locations shown in Fig. 1. SCT drifters provided usable data between 4–20 July before losing signal or beaching, while Pacific Gyre Microstar drifters provided usable data between 4–27 July, after which they either ceased transmitting, entered PWS, or advected 100 km downshelf and beyond the range of our analysis. The two SCT drifters at MID1 beached almost immediately and are excluded from the analysis. GPS location accuracy of the SCT and Microstar drifters are 5 m and 2.5 m, respectively. Drifter velocities were determined using time elapsed between consecutive GPS fixes. Drifter data was binned hourly and paired with coincident wind data from the ERA-5 spatial average. Wind and surface current velocities can be related by the function:

$$\mathbf{u} = \alpha\mathbf{V} \quad (3)$$

Where $\mathbf{u}$ and $\mathbf{V}$ are complex vectors of surface current and wind velocities respectively and α is a complex coefficient determined by least square regression (Thomson & Emery, 2014a).

2.6. True-color satellite data

Twenty years of true-color satellite imagery revealed snapshots of the CR plume spatial structure on cloud-free days. Moderate Resolution Imaging Spectroradiometer (MODIS) true-color images at 250 m resolution (2048 x 2048 pixels) using the 620–670 nm wavelengths (MODIS

Science Team, 2017) and collected by NASA's Terra and Aqua satellites between 2002 and 2021 were downloaded using the EarthData portal (Earth Science Data Systems, 2023). The satellites passed over once per day at ~ 10:00 UTC (Terra) and ~ 13:00 UTC (Aqua). The images show light green and muddy brown waters due to the CR mud and glacial flour discharging from the river mouth.

Images with appreciable cloud cover were discarded using the following filtering techniques. We required that the MODIS cloud fraction be < 50 % and we then selected the daily image registering the lowest proportion of cloud cover. A land mask was applied, along with an additional cloud filter of the red channel using a pixel intensity cutoff value of 125 (range 0 to 255). Images with faint cloud contamination, wildfire smoke, or aeolian dust from the CR delta were removed by manual inspection. An initial dataset of 402 usable images was assembled from March-October after also removing November-February images that were unusable due to low sun angle color tints. A subset of 56 images coincided with high river discharge events (Section 2.3). Analyses were based on green channel intensities normalized to a dynamic range of 0 to 255 in all images.

We use the manipulated green channel data as a proxy for sediment and freshwater distributions in the CR plume region, although this relationship is complicated due to differences in freshwater dispersal versus particle motions. Some of the sediment load settles out of the plume prior to mixing with ambient salt water, adding uncertainty to the sediment-freshwater relationship; however, clays can remain in suspension for the time/length scales associated with this study (see supplementary text), based on total suspended material (TSM) concentrations in the Copper River plume (Feely et al., 1979), the optical depths of remote satellite sensing (Loos & Costa, 2010), and the time scale for clay sized particles (diameter less than 4 μm) to sink beyond the depth of optical penetration. Using Stoke's Law a 4 μm spherical particle requires roughly 1 day to sink 1 m; the optical depths within the plume are ~ 1–5 m near the river mouth and ~ 20 m near the plume edge. Near the river mouth a reduction in pixel intensity is partly due to particles sinking below 5 m, assuming particles remain there for 5 days. Near the plume edge some particles are still visible to satellite imagery as the residence time of the plume in the CR region is likely less than 14 days (estimated from our drifter data) and particles can be detected by satellites down to ~ 20 m. We assume that the dilution of mud and glacial flour in the CR region and far (>40 km) from the river mouth in summer and fall is primarily due to mixing with ambient saltwater rather than local particle sinking and deposition. Nearer to the river mouth (<40 km) the dispersal of mud and glacial flour is due to both mixing and particle sinking.

A Self Organizing Map (SOM) algorithm using the MATLAB SOM Toolbox (Vesanto et al., 1999) was applied to the subsampled, normalized, green channel datasets (128 × 128 pixels). SOMs are pattern recognition and classification tools (Kohonen, 1982) that have been applied to many fields of study, including oceanography (Chen et al., 2006; Fang et al., 2017; Liu, 2005; Sandy et al., 2022; Tennant, 2004). They are ordered, nonlinear, artificial neural networks that do not require user-specified target training sets but do rely on iteratively determined user-defined parameters. A desired number of map elements is specified, and the SOM follows a learning rule to iteratively modify weights as the map set emerges. Data is classified according to the best-matching map element as determined by Euclidian distances between each satellite image and the map set (Thomson and Emery, 2014c). The Euclidian distance provides a measure of the error associated with each pattern's fidelity across the whole suite of images. Each pattern is thus associated with a compilation of satellite images, the main features of which are depicted by the pattern. A four-element map set was specified in the SOM algorithm for the full 402-image dataset used to describe seasonal plume patterns and then again for a second analysis based on the 56-image high streamflow dataset.

Despite the uncertainties associated with sediment dynamics, MODIS images from 29 June 2019 and 15 July 2020 were used to find a statistically significant relation between remotely sensed color and ship-measured salinity.

2.7. Tides

Near to the Copper River, the average NOAA predicted diurnal tidal range at Hinchinbrook Entrance (station 9454329) is ~ 3.4 m. This tidal range suggests that tides are likely an important factor in mixing and stratification in the CR region given the tidal influence apparent at other ROFI systems (e.g. De Boer et al., 2009; Verspecht et al., 2009). Using the M2 and S2 constituents from the NOAA tidal predictions (NOAA, 2024) we constructed a spring-neap tidal cycle for a basic assessment of tidal influence. The spring-neap cycle was compared to the average pixel intensity calculated within a 40 km square bounding box centered at 60.23 °N, 145.23 °W near the CR mouth for each March-October satellite image. The resulting linear regression had no significant relationship and including the next two largest tidal constituents (K1 and O1) did not change these results. A high resolution ROMS model shows that within the CR region the M2 tidal ellipses decline from ~ 20cm/s between the barrier islands to ~ 5 cm/s at 10 km offshore (Danielson et al., 2016) where our study took place. These factors suggest that the spring-neap tidal influence is at least secondary to wind conditions and river discharge in determining the CR plume's color, position and baroclinic current velocities in July within our study region. Concerning daily tidal oscillations, a half tidal cycle advective scale of about 0.2 m/s * 6 hr * 3600 s gives a 4-km semidiurnal length scale, which is smaller than the distance between our main survey stations and between our Acrobat survey grid lines. Thus, we are incapable of well resolving the local effects of tidal straining. Our surveys alias the semidiurnal and diurnal tides but their influence tends to average out over multiple occupations of the same transect.

2.8. Assessing plume front dynamics

The effect of an upwelling wind stress on the CR plume was estimated using theory developed by Fong and Geyer (2001) and modified by Lentz (2004). The approach relates observed initial plume conditions prior to an upwelling wind stress to theoretical advection and mixing during an upwelling wind stress. This two-dimensional model assumes plume processes are determined by a competition between buoyancy-driven geostrophic adjustment and wind driven mixing, and is based on estimates of an initial plume state, alongshore wind stress, Coriolis parameter (at 60°N), and a bulk Richardson number (Lentz, 2004). In our case, initial conditions were taken from the Middleton Line Acrobat transect on 11 July 2020. The plume boundary, defined by the 29 isohaline in both the vertical thickness and horizontal extent, was used to calculate a thickness of 10 m and a cross-shore width of 16 km. The 29 isohaline was selected because it outlines the mid-lower portion of the plume pycnocline and approximately bounds the modelled CR plume shown in Wang et al (2014) that was defined by tracer concentrations. An ambient density (ρ_a) was calculated from a section bounded by the 10–20 m depth range and 6–26 km from station MID1; a density anomaly of 5.9 kg/m^3 was computed between the plume density (ρ_p) and the ambient density.

A plume front driven by upwelling wind stress may contribute to vertical and horizontal nutrient fluxes that promote phytoplankton production and influence community structure. We seek a simple relation for silicic acid concentration changes in the CR region. The rate at which the plume area increases is described in Lentz (2004) using the relationship:

$$\frac{\partial A}{\partial t} \approx \frac{\tau_x}{2\rho_a f}\sqrt{\mathrm{Ri_b}} \tag{4}$$

Where $\mathrm{Ri_b}$ is the bulk Richardson number, τ_x is the alongshore wind stress, A denotes the area under consideration, and f is the Coriolis

parameter. The bulk Richardson number can be calculated from $Ri_b = ((g/\rho_a)*(\rho_a - \rho_p))/(\Delta u)^2$ where g is gravity and Δu is the velocity difference between ambient waters and the plume (Fong & Geyer, 2001). Based on our calculations of geostrophic currents and drifter velocity observations, we estimate that the velocity difference is between 0.2–0.3 cm/s and find Ri_b to have a range of 0.63–1.4 so select a value of 1. Wind stress is estimated from ERA-5 wind velocities following Large and Pond (1981). Entrainment occurs initially at the seaward plume front (Fong & Geyer, 2001; Lentz, 2004) after which we assume property concentrations are mixed into the entire plume volume as the entrained fluid circulates (Houghton et al., 2004). If we ignore non-conservative transformations we can use a simple mixing relationship to estimate the modified concentration of a nutrient or salt:

$$C_f = \frac{(C_p * A_p) + (C_a * A_e)}{A_p + A_e} \quad (5)$$

Where C is a nutrient concentration or salinity, and the subscripts f, p, a and e refer to final, plume, ambient, and entrained respectively. A_p and A_e represent the plume volume and entrained volume, respectively, given by a time integral of Eq. (4), (i.e. $A_e = \int \frac{\partial A}{\partial t} dt$) using hourly steps. Equation (5) was iterated for the duration of upwelling wind stress with a time step of 1 h. Negative gradients in wind stress were assumed to add zero areal extent and leave plume concentrations unchanged.

All initial plume state parameters were estimated from the 2020 process study. The greatest source of error in Eq. (5) is likely the unknown variability in entrainment depth. Model sensitivity is assessed using concentrations from 10 m and 20 m depths within the ambient section. Ambient concentrations were calculated from the horizontally averaged 10 m and 20 m Acrobat salinity observations (29.8 ± 0.8; 31.1 ± 0.2, n = 21 for each depth) between MID2-4, and silicic acid CTD bottle samples from 10 m and 20 m depths (4.6 μM ± 0.1; 4.9 μM ± 0.6, n = 3 for each depth). The initial plume values were calculated inside the 29 isohaline plume boundary for salinity (23.5 ± 4.6, n = 127), and as the mid-point of near surface (~3 m) and 10 m bottle depths at MID1 for silicic acid (19.6 μM, n = 2). The model output was compared to Acrobat salinity observations (28.2 ± 0.6, n = 149) from the 4–8 July 2019 plume also bounded by the 29 isohaline, and silicic acid (9.5 μM ± 1.6, n = 6) by the averaged MID2-4 near surface and 10 m bottles. Error in Acrobat CTD tow measurements also accounted for potential baroclinic semi-diurnal tidal advection by shifting the sections defined above ± 2 km (maximum possible displacement over a half tidal cycle given tidal current speeds). The collection and analysis of silicic acid followed GO-SHIP Repeat Hydrography procedures (Becker et al., 2020) during both process studies. Further details can be found in Ortega et al. (in review).

3. Results

3.1. NGA fresh water distributions

Using ship-based CTDs, we assessed the upper ocean seasonal freshwater cycle across the NGA study region (Fig. 1). For the upper 50 m of the water column, over the entire domain, we observed seasonal shifts in FWH, which increased from μ = 2.83 m (σ = 0.88 m), to μ = 3.73 m (σ = 1.92 m) and μ = 5.27 m (σ = 2.97 m) for spring, summer, and fall, respectively (Table 2). A fall peak in FWH is expected for the NGA shelf, when the seasonally accumulated coastal runoff in the water column contributes the most to FWH (Royer, 1982). The FWH was also highest in fall when considering each of the four individual focal study areas (Seward Line, Middleton Line, Kodiak Line, and PWS), (Table 2). PWS had the highest FWH on average throughout the year and experienced the greatest seasonal increases in FWH from spring to fall (μ = 4.03 m to 9.54 m) due to a combination of coastal discharge from surrounding glaciated terrain and topography that constrained exchange with the open ocean. In contrast, the three shelf transects, had similar mean FWH in spring, μ ~ 2.5 m (Table 2), and only the Seward and Middleton lines appreciably freshened from spring to summer, although all three lines freshened from summer to fall (Table 2). Freshening along the Seward and Middleton lines was mainly due to changes at coastal stations, which are more directly impacted by freshwater increases from adjacent melting snowfields and glacial ice (Beamer et al., 2016), while the increased FWH along the Kodiak Line in fall was due to the advection of low salinity waters carried at least in part by the ACC from the central and eastern sections of the NGA (Stabeno et al., 2016). The greatest seasonal increase in FWH for the three shelf transects was observed along the Middleton Line from spring to summer, and from summer to fall, with an increase of ~ 1.1 m (Table 2), likely due to its proximity to the large CR discharge source and other fluvial inputs southeast of the study area. This proximity to the CR heavily influenced the FWH at station MID1 (nearest to the river mouth), which peaked in summer (Fig. 3) rather than in fall reflecting the fact that the CR typically experiences peak discharge in July and its streamflow decreases by at least 50 % by September (Fig. 2). However, mid-shelf stations along the Middleton Line (e.g., MID4 and MID5) appeared to be less directly affected by the CR discharge cycle, and experienced FWH maxima in fall (Fig. 3) influenced by low salinity ACC water advecting northwest from Kayak Island, (Royer et al., 1979; Stabeno et al., 2016) combined with CR water that accumulates on the shelf throughout the summer.

Fig. 3 highlights seasonal cross-shelf FWH distributions showing that the system is more complex than a simple 2D dispersion of low salinity water, with gradients in FWH reflecting the combined effects of cross-shelf dispersion and along-shelf advection. For example, the Kodiak Line had a broadly dispersed fall FWH with a cross-shelf gradient of only −0.17 m over the first 50 km, whereas the Seward Line and Middleton Line had values of −1.75 m and 0.56 m, respectively, for the same distance and season. The Kodiak Line also often had less FWH than the Seward Line at similar distances from shore in summer and spring (Fig. 3), suggesting enhanced seaward transport of freshwater near the Seward Line compared to the Kodiak Line during these seasons. In fall along-shelf advection of low salinity water from the Seward Line, carried in part by the ACC, influenced cross-shelf distributions of FWH along the Kodiak Line. Some points of along-shelf freshwater advection on the Middleton Line persist throughout spring to fall, as shown by mean spring-fall FWH at station MID7 (μ = 3.93 m, σ = 1.70 m), which was consistently higher than FWH at station MID6 (μ = 2.93 m, σ = 1.50 m); a *t*-test (alpha = 5 %) indicates a significant difference (μ = 1.00 m, σ = 1.04 m) ($t(8) = 2.85$, $p = 0.01$) between the two that implies along-shelf advection of freshwater from southeast of the study region influencing FWH at MID7.

The density-driven velocity field contributed to the freshwater

Table 2
Freshwater height (m) as the mean (μ) +/- standard deviation (σ) for all stations on the indicated transects, Prince William Sound, and across the NGA domain.

Date Range	Seward μ ± σ	Middleton μ ± σ	Kodiak μ ± σ	PWS μ ± σ	NGA μ ± σ	Δ Seward	Δ Middleton	Δ Kodiak
4/19–5/9	2.55 ± 0.45	2.60 ± 0.43	2.41 ± 0.23	4.03 ± 0.57	2.83 ± 0.88	1.69	−0.28	0.39
6/30–7/17	2.92 ± 0.84	3.71 ± 1.59	2.55 ± 0.17	6.81 ± 1.67	3.73 ± 1.92	2.98	5.08	0.51
9/1–9/26	3.38 ± 1.69	4.85 ± 1.50	3.43 ± 1.00	9.54 ± 1.47	5.27 ± 2.97	6.28	2.48	2.70

* Difference (Δ) columns show the freshwater height range between the most nearshore station and the most offshore station. Rows denote seasons. Statistics here represent data from 2018 to 2021.

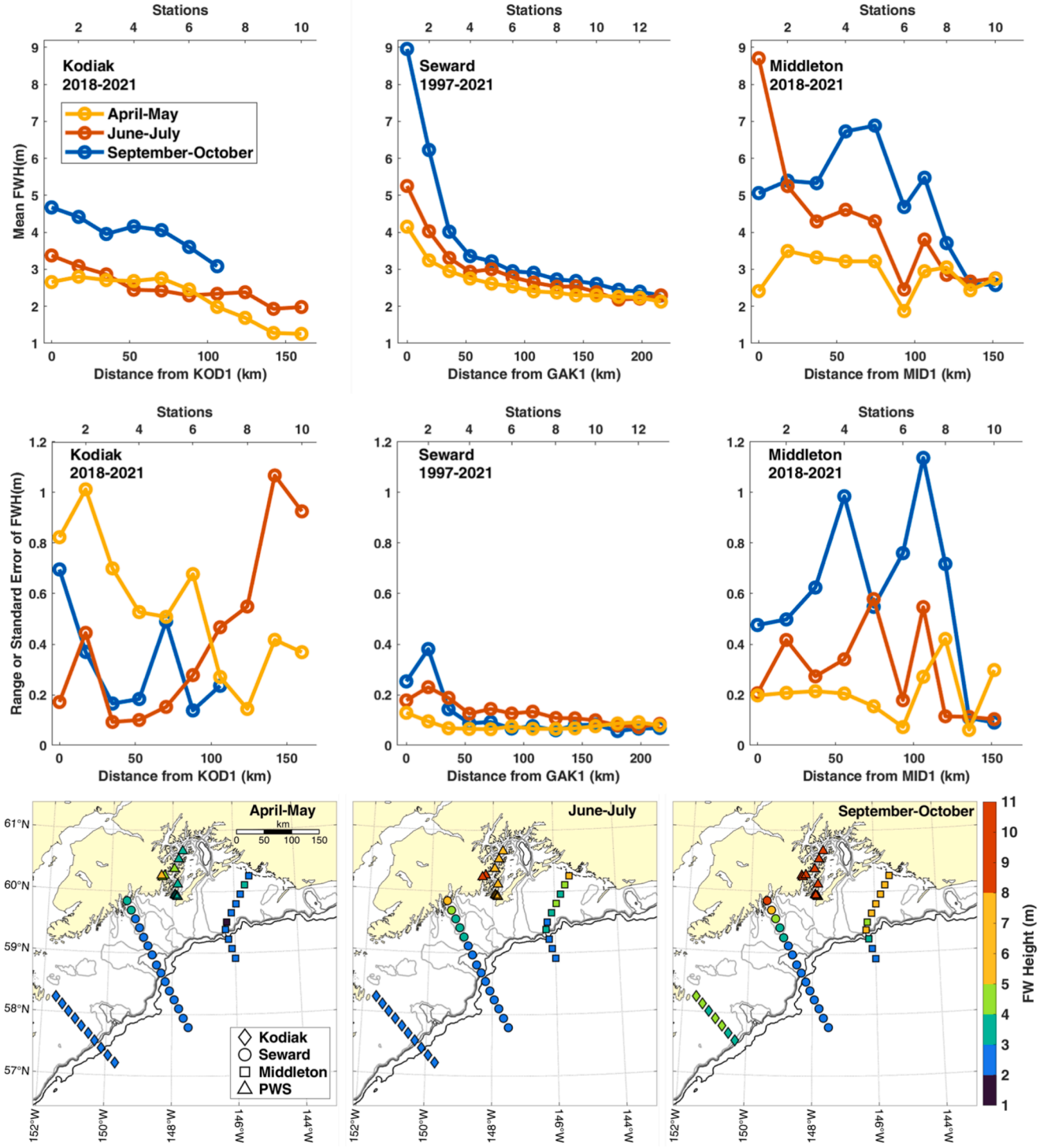

Fig. 3. Top row: Mean freshwater height computed over the upper 50 m of the water column for Middleton, Seward and Kodiak stations in April-May, June-July, and September-October for all available years of each transect. Middle row: Standard error for Middleton and Seward lines and range of observations for the Kodiak Line (the latter because the Kodiak Line was less frequently sampled than the others). Bottom row: Mean freshwater height distributions for the Northern Gulf of Alaska for April-May, June-July, and September-October (2018–2021). Bathymetric contours from light grey to black depict the 175, 250, 325 and 1000 m depths. Note that top and middle rows for the Seward Line include data from 1997 to 2021, while the bottom row only includes 2018–2021 station data for all three transects.

distribution along the Middleton Line, where averages of fall hydrographic transects show the accumulation of low salinity water near the coast and then another buildup in the mid-shelf (Fig. 4). The corresponding geostrophic velocity, referenced to 500 dbar, shows westward currents located nearshore and at the outer shelf with energetic maximum speeds of ~ 0.5 m/s to the west and lower speeds in the mid-shelf region that allow low salinity waters to accumulate. Alongshore baroclinic mass transports in the nearshore region (8–43 km from MID1) for all occupations of the Middleton Line were highest in fall of 2019 and 2021 and are westward-directed for the majority of occupations (Fig. 5). The baroclinic mass transport was also calculated from the Acrobat data during summer 2019 and 2020. Differences between the Acrobat and

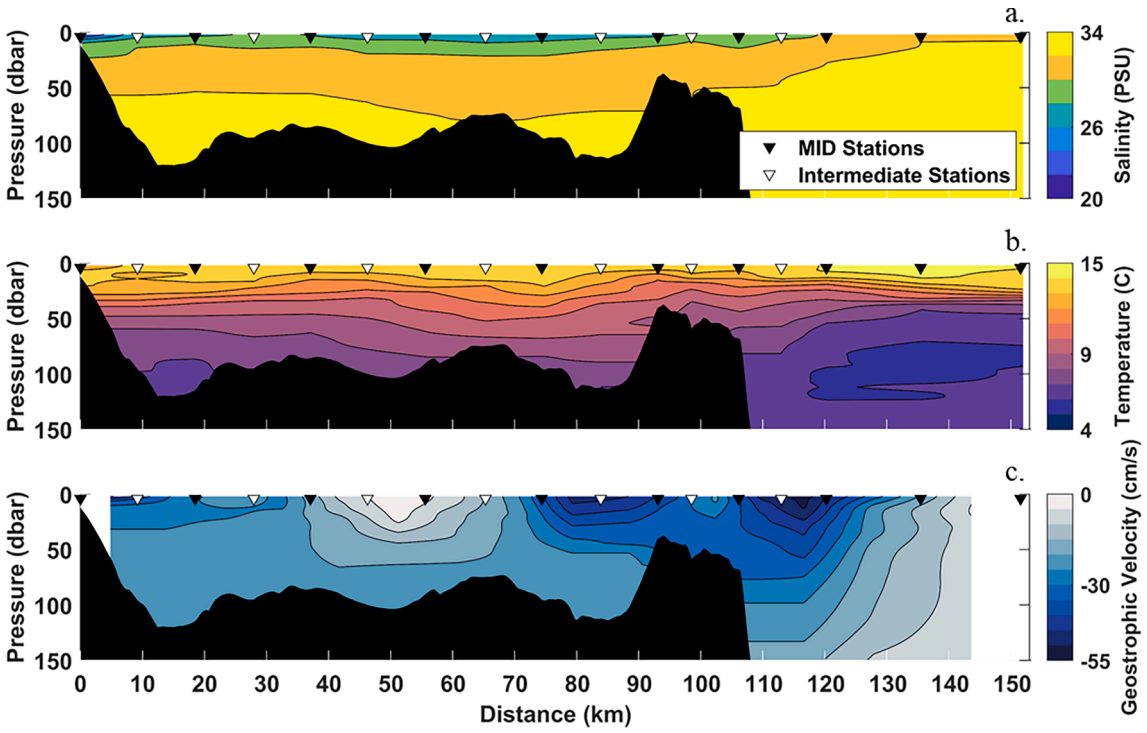

Fig. 4. Average Middleton Line distributions of (a) salinity, (b) temperature and (c) geostrophic velocity referenced to 500 dbar for fall 2018, 2019, and 2021. Horizontal axis shows distance measured from station MID1. Black triangles show the primary Middleton Island CTD station locations. White triangles denote additional CTD cast locations between the primary stations.

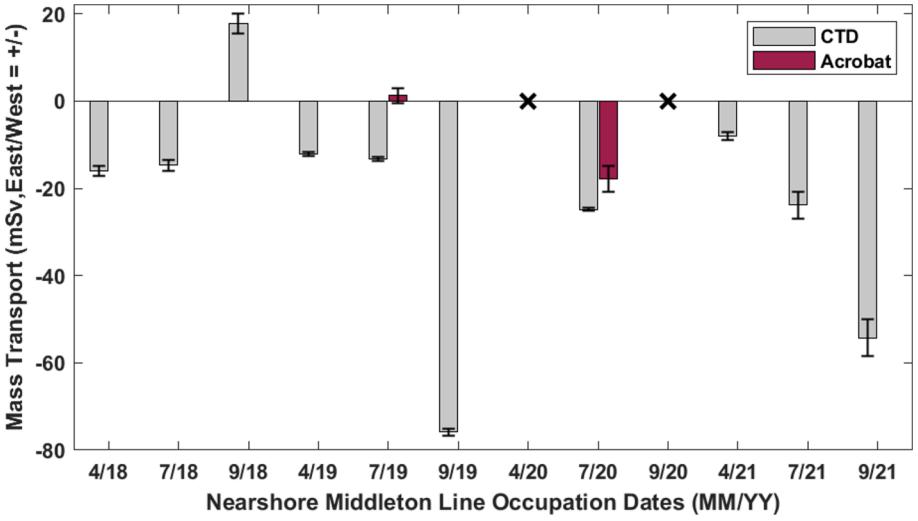

Fig. 5. Alongshore baroclinic mass transport referenced to 45 dbar for ten occupations of the Middleton Line. Transport is computed between 8 km to 43 km from MID1 using ship-based CTDs and Acrobat data (when present). Error bars denote sensitivity to tidal aliasing, estimated by shifting the CTD casts by 2 km to approximate potential tidal displacement effects.

CTD mass transport estimates may have been due to the time separation between the transects (~3 days in both years). In 2019 an additional factor may have been the presence of upwelling-favorable winds.

Seward Line CTD data (1997–2021) reveal recurring locations of low-salinity anomalies that suggest the existence of a persistent freshwater pathway near station GAK5 that appears in summer and fall. Salinity data over 0–100 m was averaged for April-May, June-July and September-October and then iteratively run in a bootstrap analysis (see Methods, Section 2.1). The 95 % confidence interval of the bootstrap distributions of mean differences between adjacent salinity gradients were used to assess significance (Fig. 6). The salinity gradient between a station pair was classified as significant if the gradient was significantly different from that of the immediately offshore adjacent pair of stations. In spring (April-May), mean lateral gradients were significantly different only for the GAK1-2 station pair. By summer (June-July), significantly different mean gradients were observed between GAK3-4, GAK9-10, GAK10-11, and in fall (September-October) GAK3-4 was again significantly different, as were GAK2-3 and GAK5-6. The changing significance at GAK1-2 from May to June-July to September-October time periods likely reflects the spatial breadth of the low salinity lens that accumulates in the nearshore region inside of the ACC front. This analysis shows that the primary ACC front location migrates seasonally and causes a

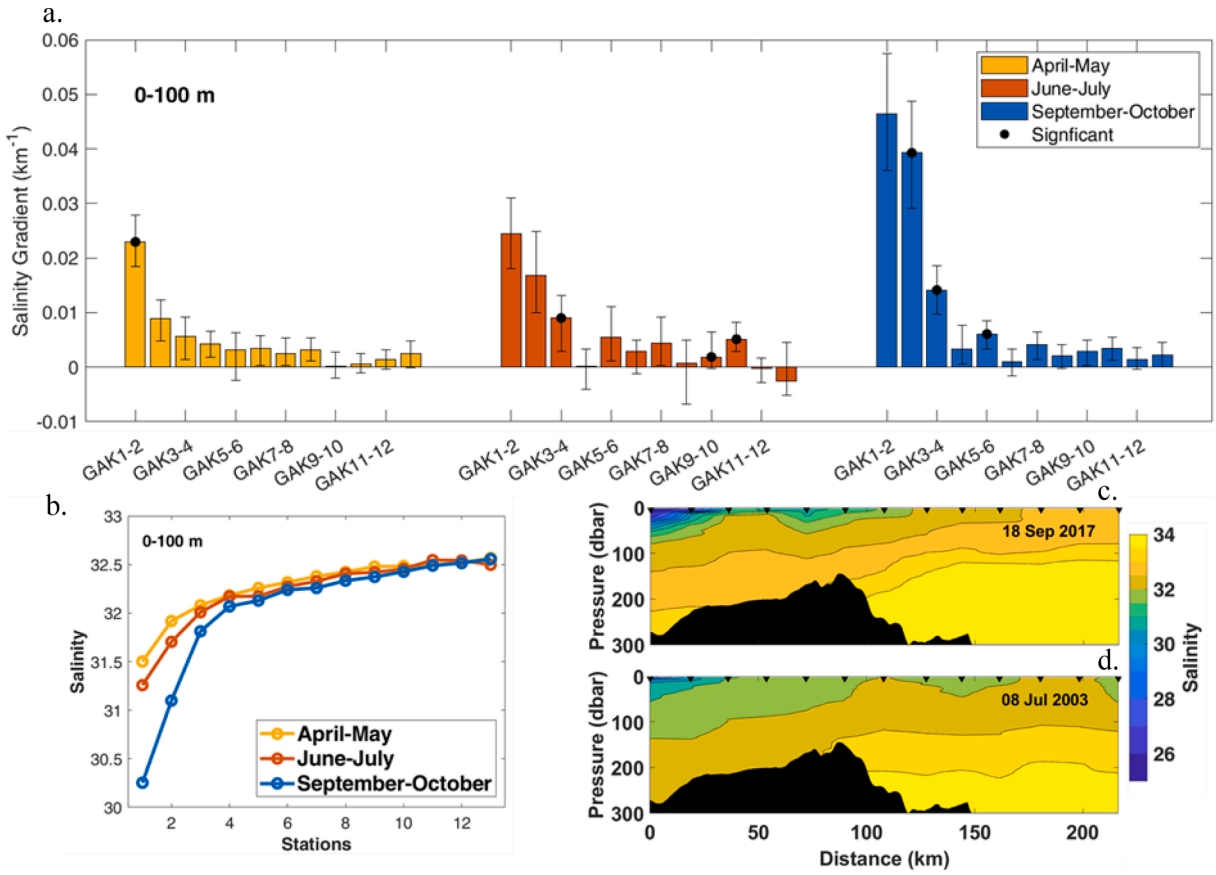

Fig. 6. Mean cross-shelf salinity gradients along the Seward Line (1997–2021), subset into April-May, June-July, and September-October, averaged across 0–100 m depths (a). A black dot at the top of a bar indicates that the mean for this station pair is significantly different from its offshore adjacent station pair (to the right), assessed using the lower and upper limits for 95 % confidence intervals in the bootstrap distribution. (b) Salinities averaged from 0-100 m for 1997–2021 along the Seward Line in April-May, June-July, and September-October. Hydrographic cross-sections of salinity along the Seward Line in September 2017 (c) and July 2003 (d) wherein distance is measured from station GAK1 and black triangles are Seward Line station locations.

persistent difference between GAK3-4 and GAK4-5. The ACC front may occasionally deflect offshore here, as the diminished gradient between GAK4 and GAK5 relative to adjacent station pairs suggests a freshwater pathway near GAK5 in summer and fall. Salinity averages by station also show this low salinity anomaly at GAK5 (Fig. 6 b) exemplified by a fall hydrographic transect (Fig. 6 c). Similarly, recurring salinity gradients during summer near the shelf break (Fig. 6a and 6d) suggest the presence of a freshwater pathway along the upper continental slope.

To summarize Section 3.1, hydrographic data from spring, summer and fall depict strong seasonality in the standing stock of coastal freshwater across the NGA. From the Middleton Line downshelf to the Kodiak Line, salinity field characteristics reflect proximity to freshwater sources and pathways by which freshwater spreads away from the nearshore zone. In particular, the Seward Line shows the likely location of freshwater pathways that are at times important for the fate of coastal waters and the offshore NGA stratification field.

3.2. Copper river plume

A key to better understanding freshwater distributions and pathways in the NGA is the salinity field time evolution, as coastal waters adjust to ambient shelf waters and the shelf circulation. The CR plume discharge intersects with shelf waters directly (as opposed to with waters in a fjord or sound) and highlights how this large surface-trapped low salinity plume propagates offshore and downshelf. Process studies of the plume physical, biogeochemical (Ortega et al. in review), and planktonic fields took place during week-long studies in 2019 and 2020. For the mapping of the physical hydrography we towed an Acrobat back and forth across the front that separated coastal and shelf waters. To assess synoptic and seasonal changes we analyzed true-color satellite imagery, river discharge data, and reanalysis wind products.

3.2.1. Wind conditions

Wind velocities (U) were downwelling-favorable ($U < 0$) during the 2020 summer process study, while the 2019 summer process study had a relatively consistent upwelling-favorable ($U > 0$) wind patten that was more unusual for the NGA (Fig. 7). The probability density function of the alongshore wind component (rotated to the principal axis of variation) during June and July for 2002–2021 shows that upwelling wind conditions matching or exceeding those observed during the 2019 process study occurred only 13 % of the time. Wind velocities matching or exceeding the downwelling-favorable conditions observed during the 2020 process study occurred 40 % of the time over 2002–2021. Strong downwelling winds form the typical summer wind pattern: upwelling-favorable conditions associated with any wind speed ($U > 0$) occurred 36 % of the time, while downwelling-favorable winds occurred the remaining 64 % of the time. Weak wind forcing ($|U| < 2$) occurred one-third of the time. All wind results were based on ERA-5 reanalysis wind data from grid points centered at 59.975 °N, 145.250 °W.

3.2.2. Plume patterns and environmental drivers

Patterns of sediment-laden waters in the CR region are extracted from processed true color satellite imagery using SOM analysis. We evaluate whether the detected colorations track the presence of low salinity plume water. Records of wind conditions and river discharge help link the plume patterns to observed environmental drivers. Finally,

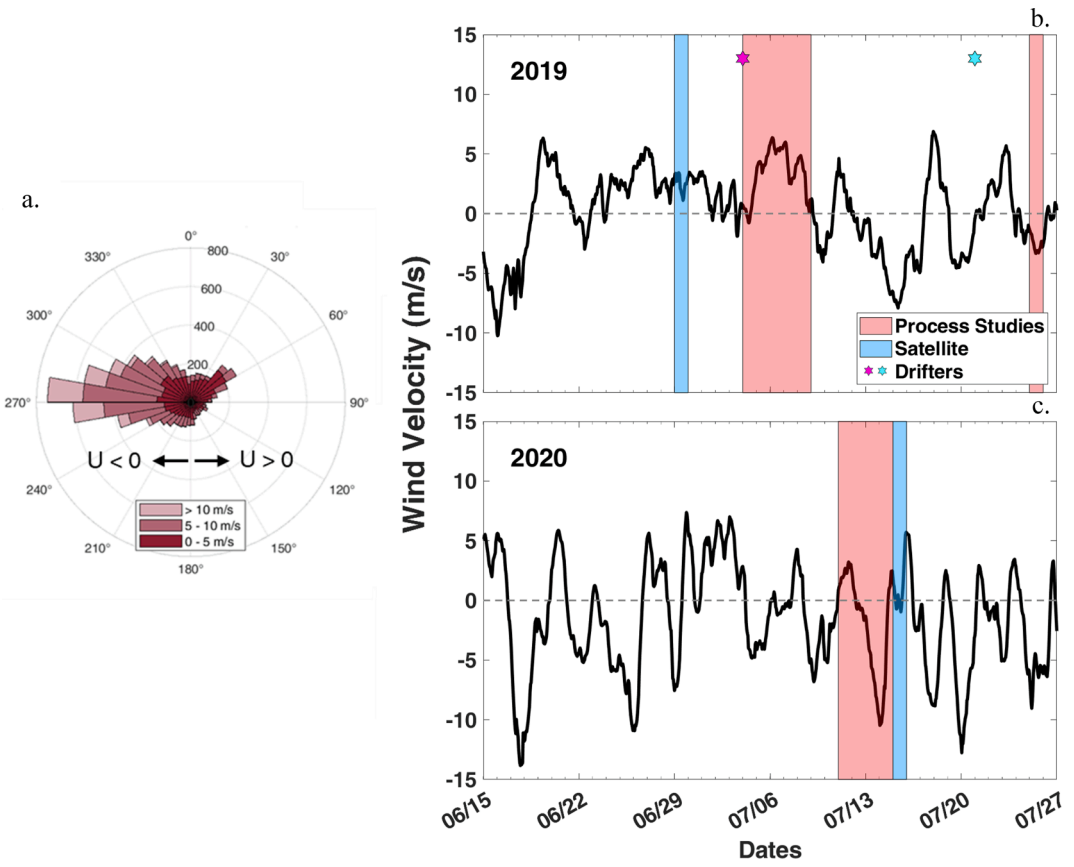

Fig. 7. (a) Wind rose for ERA-5 24-hour average windspeeds in the CR region (2002–2022) with arrows showing rotated downwelling-favorable (U < 0) and upwelling-favorable (U > 0) wind directions. (b) Hourly alongshore wind proximate to the 2019 process study. Dates are indicated for process studies (pink highlight), satellite image timestamp (blue highlight), drifter deployment (magenta star) and final transmission of the longest surviving drifter (cyan star). (c) Same as (b) but proximate to the 2020 process study.

the analysis is repeated for a dataset with a relatively constant river discharge to investigate the effect of wind conditions on the plume.

Based on satellite images collected between March and October, a 4-pattern SOM analysis reveals dominant patterns of sediment-laden waters in the CR region. Anomaly maps constructed from the four patterns (Fig. 8 a, bottom row) show pixel intensities relative to the average, based on the true-color images' green channel (see Methods, Section 2.6). SOM pattern A depicts sediment-laden waters distributed across the study area, and a somewhat weaker intensity near the river mouth. Pattern B shows the plume oriented downshelf toward PWS. Pattern C suggests elevated concentrations of sediment close to shore west of the river mouth and entering PWS via Hinchinbrook Entrance, sediment flowing past Kayak Island, and a notable decrease in plume intensity offshore and west of the CR mouth. Pattern D suggests less turbid waters across the study area. All patterns exhibit some seasonality. Pattern A makes up 50 % and 19 % of March and April, respectively, and < 6 % for each month from May to August, while pattern B images make up < 6 % in March and April and > 23 % for each of the remaining months (Fig. 8 b). From inspection and comparison to the original true-color imagery, the SOM patterns capture common surface expressions of sediment laden waters in the CR region from March to October.

Towed CTD surface salinity measurements from repeated crossings of the CR plume boundary suggest that sediment color in the satellite images provides a useful proxy for salinity and freshwater distributions near the river mouth (Fig. 9). During the 2020 process study, for each of the 5 km binned Acrobat data points that were not overlaid by clouds, a three-by-three set of image pixels was averaged to obtain the corresponding satellite image pixel intensity (Fig. 9 b). Linear regression of the green channel intensity explained 66 % of the ship-based surface salinity variance in 2020 (Fig. 10) in an image that was obtained one day after the process study hydrographic mapping was complete. The portion of the plume that is most visible on the western side aligns with *in situ* samples taken ~ 48–30 h before the satellite image was captured. Linear regression to the 2019 sea surface salinity data resulted in a much weaker relation to green channel intensity (21 % of the variability explained) reflecting the nearly 5-day gap between a sufficiently cloud-free true-color image and the *in situ* measurements (Fig. 9 a). As such, the 2019 data is not collectively considered with 2020 in determining a pixel intensity to surface salinity relationship (Fig. 10). Based on these analyses, sediment colored waters can serve as a proxy for freshwater distribution during summer in the CR region. This relationship may be extended to fall although contamination from resuspension in the very nearshore may degrade the relation. Images from spring contain sediment and ocean color gradations that do not appear to be closely related to freshwater distribution

To assess the influence of environmental forcing on the plume, we grouped images based on coincident alongshore wind velocity and river discharge conditions. Tests for equal variance between pattern groupings (A-D) show that variances in wind data are equal between groups, and the same is true for discharge data (Fig. 11 a). One-way ANOVA tests assessed the individual importance of alongshore wind velocity and river discharge on each pattern (Table 3 a). These signifigant relationships depicted in Table 3 indicate that SOM plume patterns can be ascribed to environmental drivers in the CR region: Pattern A is associated with weakly downwelling favorable wind; Pattern B is associated with high river discharge and upwelling favorable winds; Pattern C is associated with downwelling favorable winds and Pattern D is associated with calm winds.

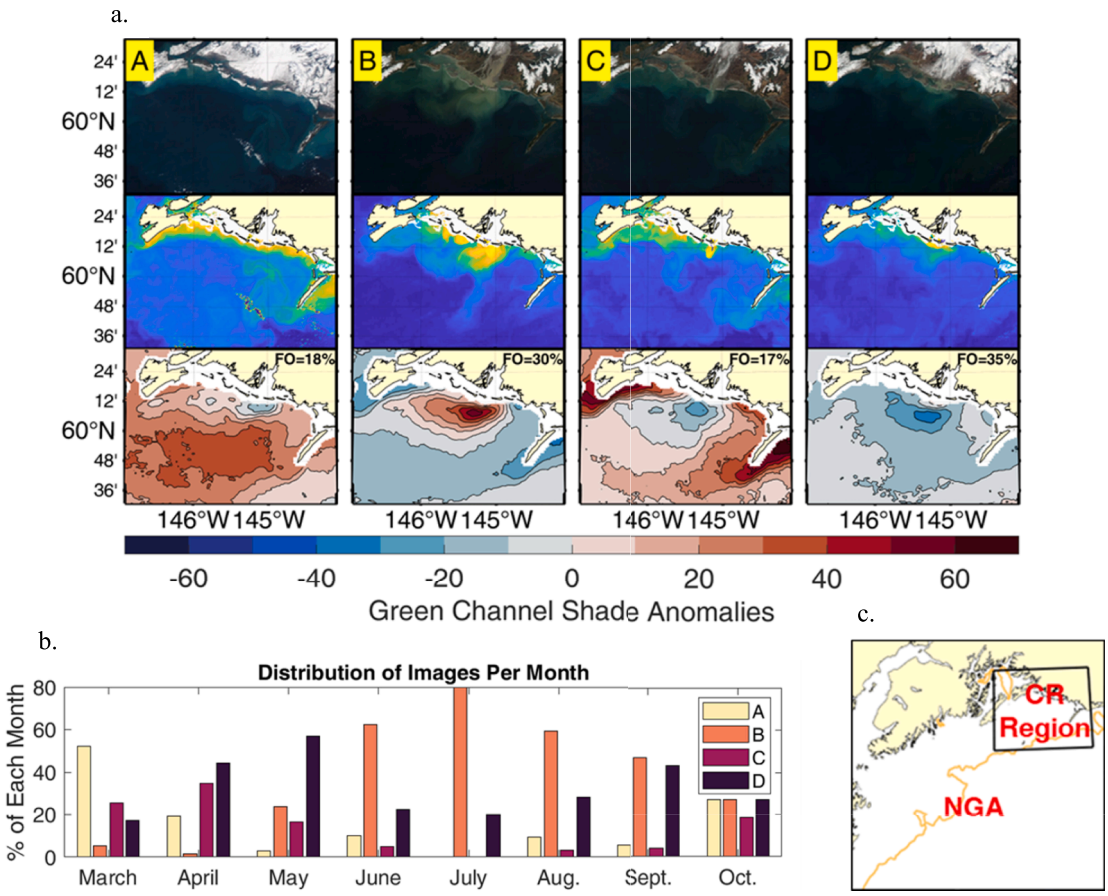

Fig. 8. a) top row: representative examples of true-color images for each plume distribution pattern in the cr region. middle row: examples of green channel processing applied to the true-color images in the top row, with colors ranging from yellow (high turbidity) to blue (low turbidity). bottom row: anomaly maps resolved by theself-organized mapping (SOM) analysis and generated by subtracting the total image collection mean from each of the four resolved SOM patterns. Frequency of Occurrence (FO) denotes the fraction (%) of images ascribed to each pattern. b) Distribution of images per month for each of the four SOM patterns. c) Reference map for CR region, shown in anomaly maps.

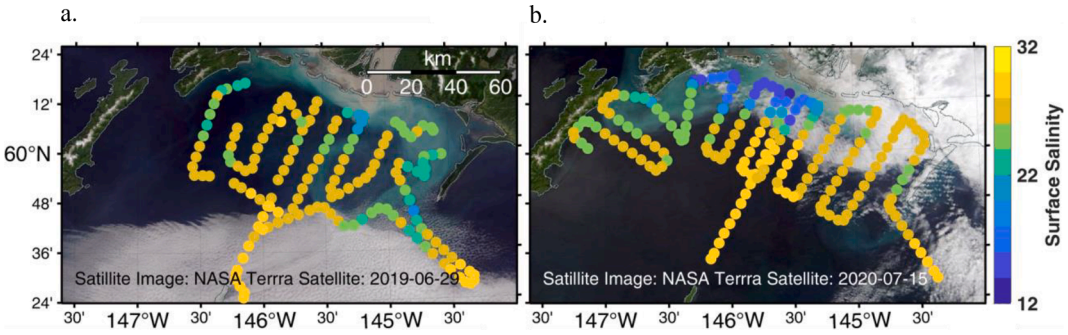

Fig. 9. *In situ* surface salinity binned to 5 km overlaying near simultaneous satellite imagery for 4–8 July 2019 (a) and 11–14 July 2020 (b) process studies.

While the SOM patterns suggest that wind affects the plume's location, the strong seasonal river discharge of the CR helps determine the overall presence of freshwater in the CR region. The influence of the river discharge on sediment color gradations and freshwater presence can be evaluted using the average pixel intensity of the seasonal set of images under calm wind conditions ($-2 < U < 2$ m/s). The average pixel intensity was calculated within a 40 km square bounding box centered at 60.23 °N, 145.23 °W. By linear regression, the river discharge explained 36 % of the variance in green channel intensity (Figure S1).

A second 4-pattern SOM analysis of the image dataset was constrained to dates exhibiting elevated river discharges only. SOM pattern E shows the plume spreading upshelf toward Kayak Island and extending south (Fig. 12). Pattern F shows relatively low amounts of sediment at the river mouth and across the study area. Pattern G shows high amounts of sediment at the river mouth and across the study area. Pattern H shows sediment constrained close to the shore in the downshelf direction.

Image collection dates were again used to assess coincident environmental conditions. Tests for equal variance between pattern groupings (E-H) show that variances in wind data are equal between groups, and the same is true for discharge data (Fig. 11 b). One-way ANOVA tests (Table 3 b) show pattern G's high river discharge ($\mu = 5395$ m^3 s^{-1}) was significantly different from Pattern F's somewhat lower river discharge ($\mu = 4329$ m^3 s^{-1}). Wind velocities exhibited no significant

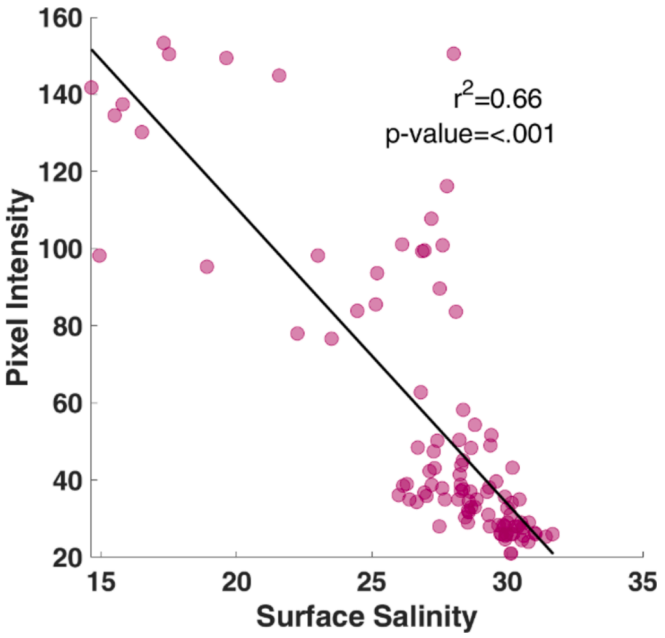

Fig. 10. Regression of satellite image green channel pixel intensity versus surface salinity in 2020 binned to 5 km along-track intervals for the data shown in Fig. 9 b (cloud-contaminated pixels excluded).

relation at $p < 0.05$, though a weakly significant diffference ($p < 0.10$) is found between Pattern E's upwelling wind velocity ($\mu = 2.3$ m/s) and Pattern F's weakly downwelling-favorable winds ($\mu = -0.8$ m/s).

3.2.3. *Baroclinic mass transport*

In-situ measurements of the CR plume in summer show how the plume functions while the CR river discharge and upwelling-favorable wind conditions are seasonally enhanced. Analysis of Acrobat data from the 2019 and 2020 process studies show that in both years westward baroclinic transport tended to occur west of the CR mouth and eastward transport to the east of the mouth (Fig. 13) despite the constrasting wind conditions. However, relatively high southwestward baroclinic transport advected along the slope, past the tip of Kayak Island, only during the net downwelling conditions of the 2020 process study, compared to very little for the same segment during the upwelling conditions of the 2019 process study. The eastward volumetric transport that occurs east of the CR mouth in both years contributes to a quasi-persistent gyre that tends to form on the shelf northwest of Kayak Island (Royer et al., 1979) and is associated with the eastward baroclinic current near the coast and on-shelf northward flow past the tip of Kayak Island (Fig. 14). The eastward flow is distributed between the surface and 40 m depth. In contrast, to the west of the CR mouth, the plume creates a westward baroclinic current with higher velocities but is constrained between the surface and about 15 m depth.

CTD and Acrobat hydrographic transects for 2018–2021 and ERA-5 wind velocities allow us to assess alongshore baroclinic transport relative to coincident wind conditions. Mean alongshore wind velocities for the CR region were calculated using the occupation time for transects 1–11 (inset Fig. 13). To constrain our transport estimates to the plume waters only, we referenced the geostrophic velocitites of these transects

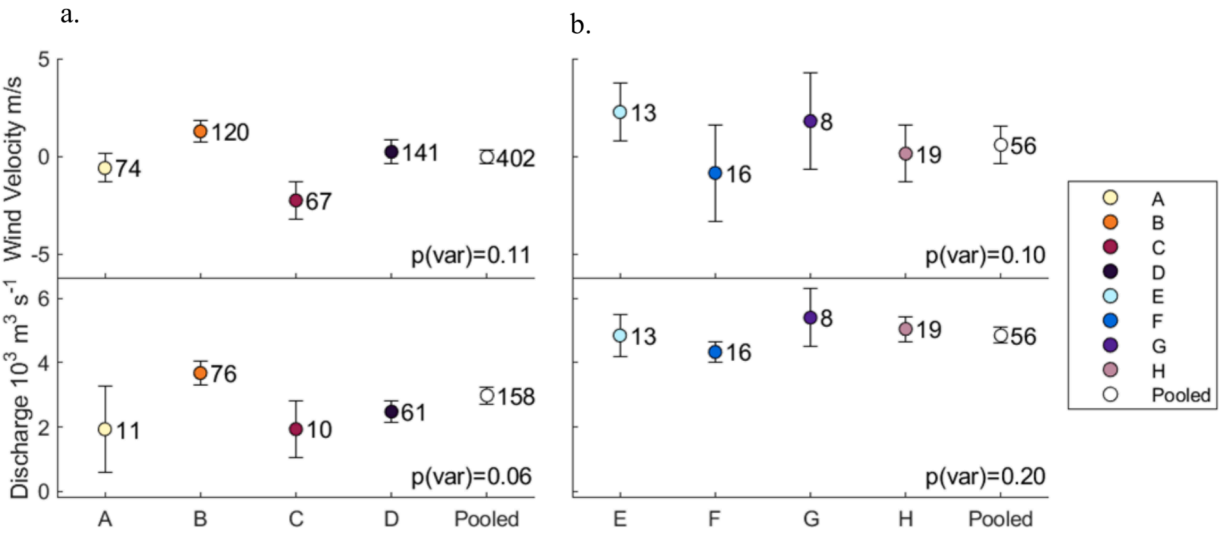

Fig. 11. (a) Mean values with 95% confidence intervals are shown for seasonal patterns A through D, as well as for all patterns combined (pooled), for wind speed and river discharge. Samples sizes are listed beside each mean, and p-values for a test of equal variances are shown in the bottom right corner of each plot. (b) Same format as (a) but using the high discharge patterns E through H.

Table 3
A: seasonal patterns multiple comparisons test for som patterns a-d.Table 3b: High discharge patterns multiple comparisons test for SOM patterns E-H.

Seasonal Comparisons	Win Velocity p-Value	River Discharge p-value	High Discharge Comparisons	Win Velocity p-Value	River Discharge p-value
A-B	<0.01	<0.01	E-F	0.09	0.39
A-C	0.02	0.99	E-G	0.99	0.49
A-D	0.34	0.69	E-H	0.33	0.92
B-C	<0.01	<0.01	F-G	0.30	0.03
B-D	0.07	<0.01	F-H	0.83	0.06
C-D	<0.01	0.72	G-H	0.66	0.77

* P-values are for a hypothesis test that the mean difference between two groups is equal to zero.

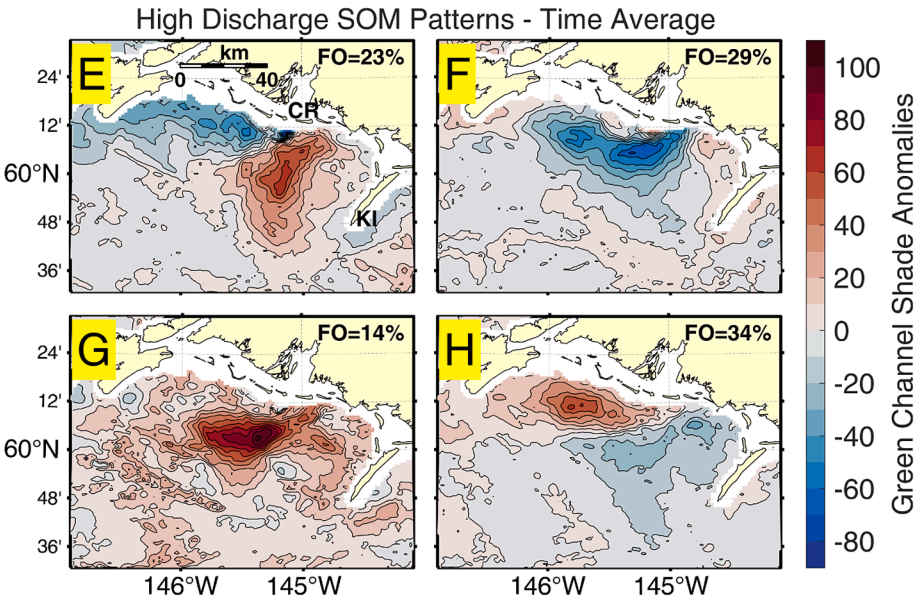

Fig. 12. Anomaly maps resolved by the self-organized mapping (SOM) analysis and generated by subtracting the image collection mean from each of the four resolved SOM patterns for instances of high discharge only (n = 56 wherein river discharges is above 2/3 of median seasonal peak).Warm colors indicate more sediment, cooler colors indicate less. Frequency of Occurrence (FO) denotes the proportion of images (%) ascribed to a particular pattern. Also shown are labels for the Copper River (CR) mouth and Kayak Island (KI).

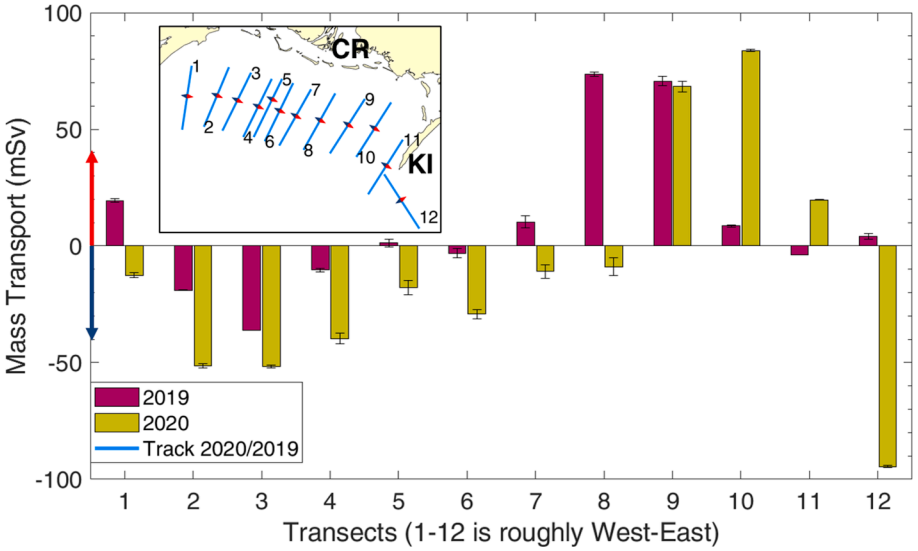

Fig. 13. Baroclinic mass transport calculations referenced to 45 dbar for the 2019 and 2020 process studies for the transects shown in the map insert. Arrows shown on the bar plot and map insert denote flow to the east (red) and west (blue). Error bars denote uncertainty due to tidal phase. Also shown are labels for the Copper River (CR) mouth and Kayak Island (KI).

to 15 dbar and calculated the baroclinic transport for 35 km sections. The results are consistent with our expectation that downwelling-favorable winds cause steepened isopycnals and lead to higher downshelf transport (towards PWS). Demonstrating the role of Ekman dynamics in controlling the plume hydrographic structure, we find that alongshore transport is moderately well correlated with alongshore wind velocity (r^2 = .47, p = <.01) (Fig. 15).

3.2.4. *Cross shelf plume tracks*

Ten drifters deployed west of the CR plume's location on the Middleton Line during July 2019 show the movement of surface water in the CR region as wind conditions shift from upwelling-favorable to downwelling favorable. To start, all drifters moved east of the Middleton Line and remained there for 7–11 days, primarily under the influence of upwelling-favorable winds (Fig. 16) and the Kayak Island gyre. Two of the circulating drifters crossed the shelf break 75 km due south of the CR mouth, showing a direct pathway of coastal waters into the iron-limited high nutrient low chlorophyll (HNLC) waters of the adjacent basin. During July 12–16 four surviving drifters, including one that had reached the shelf break, return north under the influence of downwelling winds and were constrained to within 25 km offshore of Hinchinbrook Island. Once drifters were west of the Middleton Line, they moved westward for 3 days at an average speed of 0.31 ± 0.05 m/s before three veered towards Hinchinbrook Entrance; one continued downshelf beyond the study area.

Drifter data reveal Ekman dynamics associated with the surface flow field independent of the underlying hydrography, which helps quantify the relationship between cross-shelf flow and wind conditions. Under

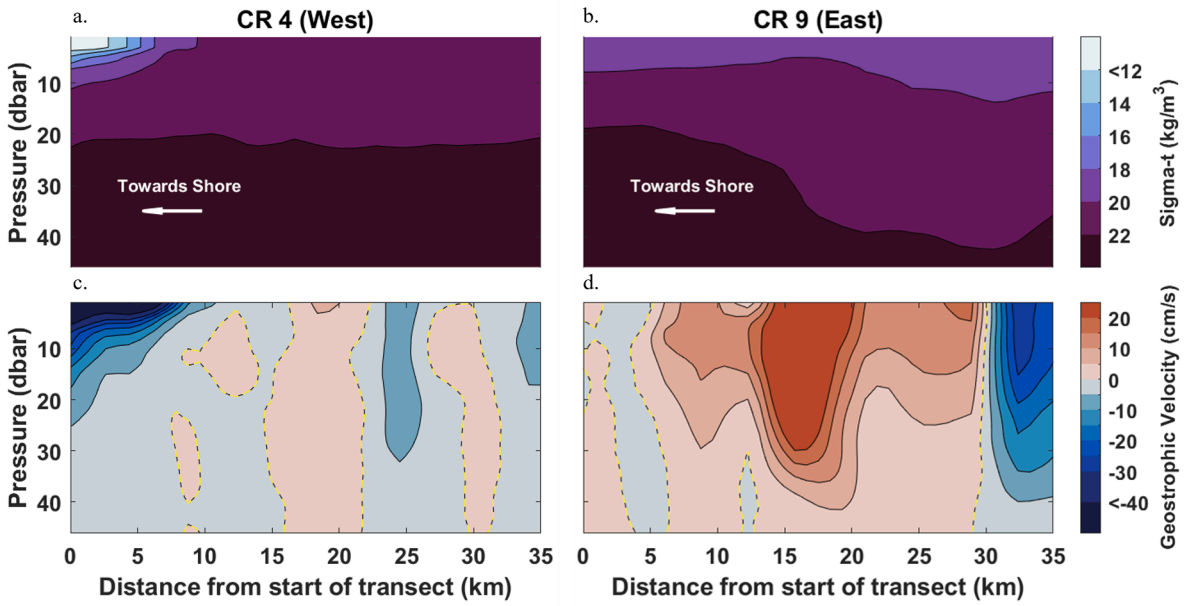

Fig. 14. Density (sigma-t; a-b) and geostrophic velocity referenced to 45 dbar (c-d) along 35 km transects starting nearshore and located west (CR 4, left plots) and east (CR 9, right plots) of the Copper River mouth during the 2020 process study. Dashed contour in geostrophic velocity plots denotes 0 cm/s; directions are approximately east (+) and west (−). Fig. 13 shows the locations of the transects CR 4 and CR 9.

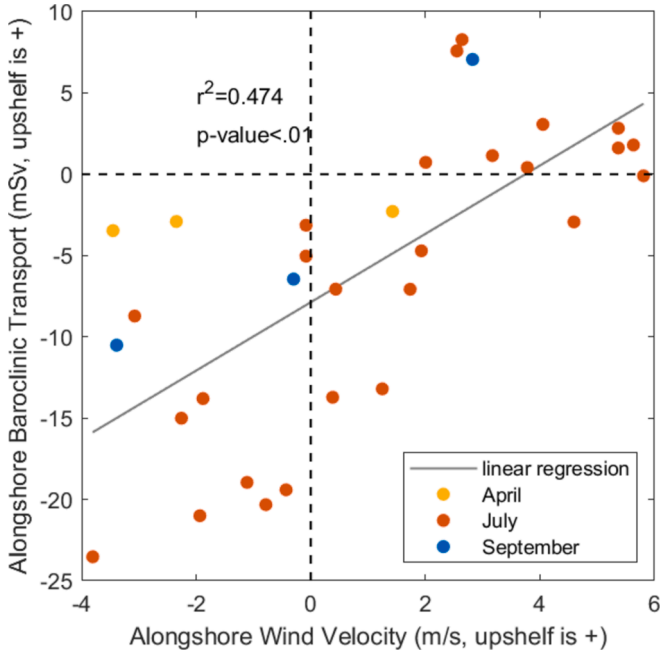

Fig. 15. Linear regression of alongshore baroclinic transport across 35 km length by 15 m depth sections near the Copper River mouth versus the regional alongshore wind speed. CTD transects and Acrobat transects were combined for the years 2018–2021. Level of no motion is 15 dbar. Regression statistics include all data points.

Ekman's theory, surface drifter motion is expected at an angle of ~ 45° to the right (clockwise) of the wind direction in the northern hemisphere (Ekman, 1905). A histogram of the difference in direction between the wind and current vectors (Figure S2) reveals a peak between 40 and 50° for downwelling-favorable wind conditions (U < 0) and a peak between 60 and 70° for upwelling-favorable wind conditions (U > 0). Following a two-parameter complex function approach to calculate current turning angles for the upwelling-favorable and downwelling-favorable wind conditions, we find angles of 48.3° ± 0.8 (U > 0) and 44.6° ± 1.8 (U < 0), where error is estimated by the range of angles calculated when winds velocities relative to the drifter times are offset by two hours. The range of turning angles measured clockwise from the wind direction for upwelling-favorable (32.8–58.8°) wind conditions were often slightly greater than the turning angles for downwelling-favorable (28.7–48.3°) wind conditions (Table S1), possibly due to directional bias imparted by the westward background flow of the region.

3.2.5. *Plume dynamics*

Cross-sections from three July occupations during 2019 and 2020 of the Middleton Line from stations MID1 to MID6 show that water with salinity < 29 is constrained to the coast during downwelling-favorable wind conditions and a typical discharge (Fig. 2; Fig. 17). The plume spreads out across the shelf during instances of upwelling-favorable wind conditions and high freshwater discharge relative to the seasonal median in July. These salinity distributions show the influence of wind on the low salinity plume waters and on the isopyncal slopes that drive baroclinic transport.

Applying the model of Lentz (2004) to our presumed initial conditions (see Methods, Section 2.8), we estimate that the alongshore upwelling-favorable wind stress between 20 June 2019 and 4 July 2019 could extend the seaward plume edge by 11 km, decrease the density anomaly between plume and ambient waters by 2.5 kg m^{-3}, and increase the plume thickness by 1.7 m. Using the 29 isohaline as the border of the plume, we observed the plume to extend seaward (Fig. 17), consistent with the expected relationship in Lentz (2004). The observed density anomaly decreased by ~ 3.5 kg m^{-3}, and the final plume thickness decreased by 5 m. The reduced plume thickness is not consistent with Lentz (2004), a possible consequence of a misalignment between the 04 July 2019 transect and the plume center.

The change in plume salinity and silicic acid concentrations can also be analyzed based on Lentz (2004). Given ambient silicic acid concentrations of 4.6–5.0 μM μM SiO_3, the same period of wind stress used to predict plume width would cause accumulated plume concentrations of 14.4–14.5 μM SiO_3. Ambient salinities of 29.8–31.1 would cause a final plume salinity of 25.7–26.0. The actual average plume values for the 2019 process study for salinity and silicic acid were 28.2 ± 0.6 and 9.5

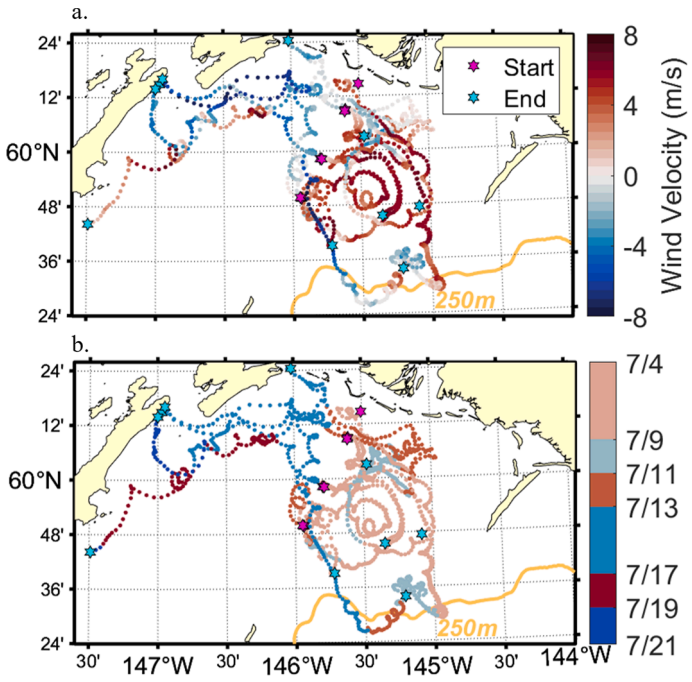

Fig. 16. a) hourly binned gps tracks for surface drifters, colored by the era-5 alongshore wind velocity. darker colors denote higher intensity winds. stars show the drifter deployment locations (magenta) and final transmission (cyan). b) same as a) but with discrete periods of upwelling-favorable (red shades) or downwelling-favorable winds (blue shades) shown in the colorbar. darker colors denote later dates. Fig. 7 b shows alongshore wind velocity for the maximum drifter timespan.

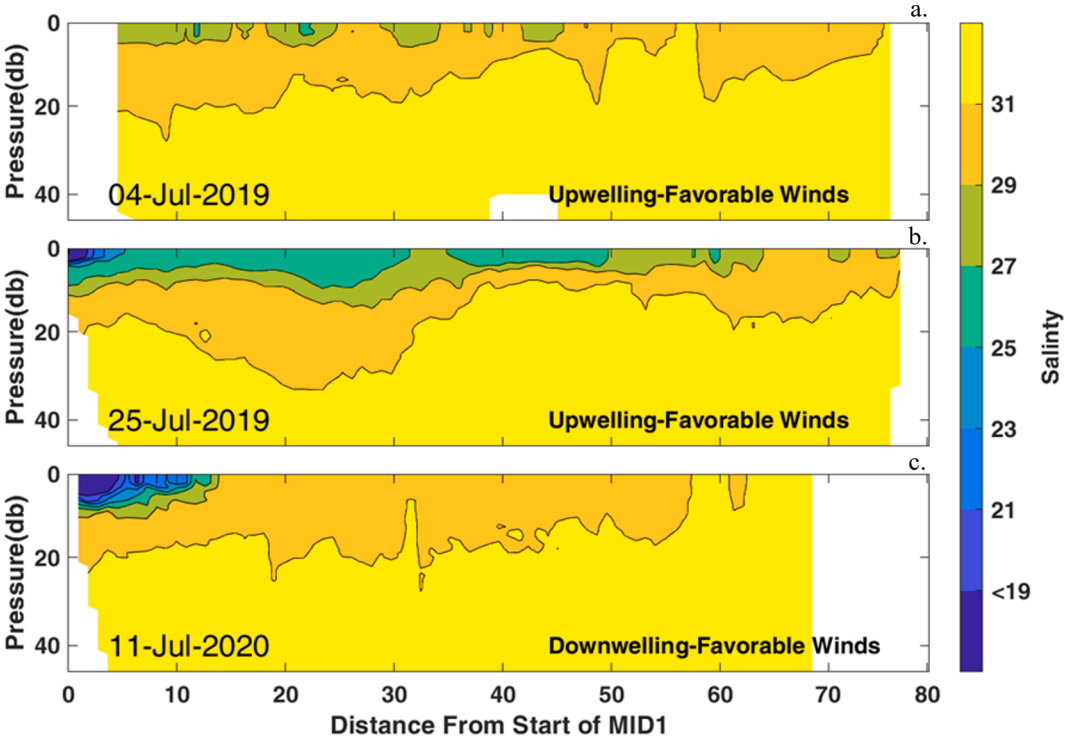

Fig. 17. CTD and Acrobat salinity transects of an 80 km section of the Middleton Line starting at station MID1. Coincident wind conditions are noted on each panel.

μM ± 1.6 respectively. This suggests that the plume initial conditions modified by dilution and entrainment due to upwelling-favorable wind conditions account for about half of the observed average silicic acid and salinity concentrations.

3.3. Freshwater pathways in the NGA

Our above results show the seasonal distributions of low salinity water in the NGA and provide evidence for important recurring freshwater pathways mid-shelf (GAK5) and near Middleton Island. In the CR region, the combined influences of upwelling and downwelling-favorable winds, the Kayak Island gyre, and ACC flows bring about a

temporally and spatially variable current field (Fig. 18). Downwelling-favorable winds cause currents that are directed generally westward, while upwelling-favorable winds cause currents near the CR to be directed upshelf or cross shelf. The gyre west of Kayak Island can be present during both wind conditions in summer. Our results in the CR region provide new perspectives on the CR plume's response to river discharge and wind conditions and explore how wind conditions alter the freshwater pathways that originate in or pass through that region.

4. Discussion

4.1. Re-assessing freshwater distributions and pathways

Freshwater height (FWH) tracks the distribution of freshwater nearshore and on the shelf in the NGA, and drives associated baroclinic transport. Wind direction and the Kayak Island diversion of low salinity ACC water modulate the low salinity waters found above 50 m depth between Middleton Island and the CR mouth (Fig. 3), while the CR discharge feeds the same area. Baroclinic transport at the Seward Line increases as low salinity water accumulates nearshore in summer and fall months. In contrast, low salinity water on the Middleton Line can more readily disperse across the shelf, the baroclinic transport is less here than across the Seward Line, and drifter data (Fig. 16) suggest that the front contains more meanders than farther west on the shelf. This latter characterization is supported by the drifter trajectories shown here, by Royer et al. (1979), Stabeno et al. (2016) and the dipole eddies (Ahlnäs et al., 1987) observed in the CR region.

Seasonal changes in FWH along the Middleton Line reflect key processes of the regional flow field, including seasonal changes in CR discharge and alongshore current strength. Higher FWH at station MID1 in summer than in fall is likely related to the CR's peak discharge in July (Fig. 2; Fig. 3) but this does not contribute much to baroclinic transport because the seafloor depth is only ~ 20 m at MID1 and we find here relatively flat isopycnals. The low salinity river water spreads as a thin surface-trapped plume in summer. In fall, Kayak Island diverts the seasonally stronger ACC, contributing to a peak in FWH at MID5. This results in a baroclinic current that flows eastward between stations MID3 and MID4. The permanence of this current is unknown, though Royer et al. (1979) shows three drogued drifters during the month of September that appear to respond to an eastward current feeding into an eddy west of Kayak Island. Between station MID5 and station MID9 a broad westward flowing baroclinic current appears to split around Middleton Island (Fig. 18). This westward current has also been found by previous drifter studies (Stabeno et al., 2016) and represents a potential source of nutrient rich basin-origin waters to the shelf.

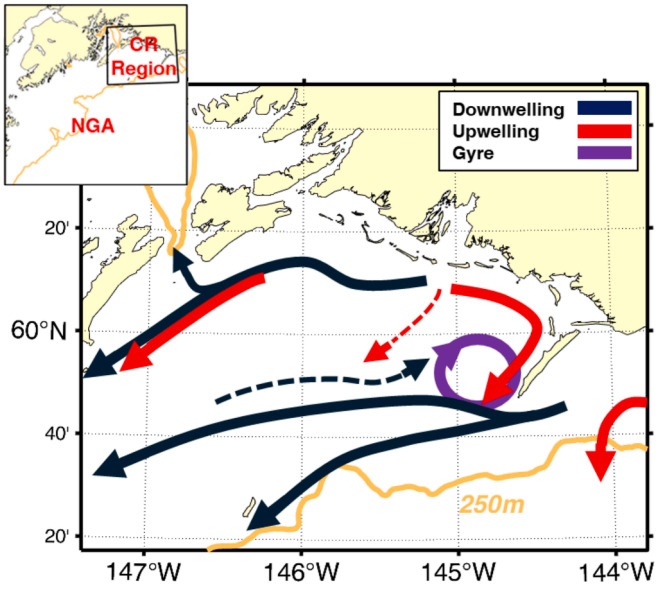

Fig. 18. Idealized schematic of potential current patterns in the CR region with mean currents under downwelling-favorable wind velocities (dark blue) including a weak counter current (dashed dark blue); and mean currents under upwelling-favorable wind velocities (red) that more often occur in summer, including offshore spreading during weak upwelling (dashed red). The Kayak Island gyre (purple) is present under both wind conditions.

Kodiak Line freshwater is more deeply mixed into the water column than the other lines in part because this line is farther from the nearest large freshwater source and because the coastline lacks continuity from the mainland. The inherent advective lag time allows the low salinity water to disperse cross-shelf (Weingartner et al., 2005), or mix into water layers deeper than 50 m. The lack of change between spring and summer FWH along the entire Kodiak Line (Fig. 3) likely reflects the advective time scale and the importance of mixing driven by strong local tidal currents over Albatross and Portlock banks (e.g., Fig. 8 of Danielson et al., 2020).

Long term data from the Seward Line help distinguish recurring freshwater pathways. Mean cross-shelf gradients of salinity in the 0–100 m layer between GAK1-5 trend towards smaller positive values seaward along the Seward Line, in accordance with increasing salinity offshore (Fig. 6 a). Sharp deviations to this trend suggest that processes other than cross-shelf eddy fluxes of freshwater (Weingartner et al., 2005) may be involved. For example, when salinity (density) gradients shift from positive to zero, this can indicate the presence of a baroclinically maintained freshwater pathway (Fig. 6 b). The significant difference between the gradients of GAK3-4 and GAK4-5 likely indicate a mid-shelf freshwater pathway near GAK5, perhaps reflecting a persistent or recurring deflection of ACC waters from the outer edge of Montague Island. A hydrographic transect from September 2017 shows a low salinity bolus near GAK5 as an example of this feature (Fig. 6 c). GAK9-10 and GAK10-11 during June-July also exhibit a gradient that could be caused by a low salinity jet at the shelf break. It spans GAK9-10 and contrasts with higher surface salinities at GAK11 (Fig. 6 d), and may reflect the development of a shelf break front driven by advective and diffusive processes (Narayanan & Garvine, 2002). Low salinity surface waters (30–31 range of salinity) observed southwest of Kayak Island at the shelf break by an autonomous underwater vehicle during a 2022 along-slope transect from east of Kayak Island to GAK13 (NGA LTER unpubl. data) suggest that this feature extends well upstream of the Seward Line.

Despite the deep bottom depths and strong stratification, processes and hydrographic characteristics shaped by shelf bathymetry are apparent even in near surface waters. For example, mixing and on-shelf advection of slope and basin waters likely causes the locally low FWH that we observed in all seasons at MID6 (the shallowest station along the Seward Line). The bathymetry west of MID6 starts at 40 m and drops to over 250 m after 10 km due to a network of steep canyons that incise the shelf break and slope to below 1000 m depths. It's possible that tidal mixing combined with topographic steering of the slope current allows high salinity, nutrient rich water to flow through MID6, similar to observations from the banks and canyons near Kodiak Island (Mordy et al., 2019). The low FWH observed along the Kodiak Line (especially at station KOD3) are also likely reflective of tidal mixing and bathymetric steering, though our observations on the Kodiak Line are more limited.

4.2. Fate of the copper river plume

Wind conditions and freshwater discharge rates appear to both contribute to the fate of the CR freshwater plume. While satellite imagery of surface sediment gradations can be a useful tool in tracking the plume, these sediment distributions must be interpreted with care because of the different factors that regulate sediment and freshwater residence times in the water column. The prevalence of pattern A in spring (Fig. 8 b) and its sediment distribution suggest that the pattern is

associated with sediments resuspended in shallow waters (within ~ 20 km of the coast) during spring storms, which are then transported to deeper waters farther offshore. Similar resuspension occurs in the region west of the Mississippi River outflow (Salisbury et al., 2004).

Some SOM patterns show the utility of our analysis approach in tracking sediment laden freshwater plumes in summer months. For pattern B, the high amount of sediment near the mouth of the CR can be related to low salinities (Fig. 9); the distribution of image dates which peak in July (Fig. 8 b) indicate that the CR discharge and the summer wind conditions are key drivers. This is supported by Pattern B's high discharge and upwelling-favorable wind conditions that are significantly different from many of the conditions associated with other patterns (Table 3 b). Additionally, prior studies have found that upwelling wind stress can detach a river plume from the coastline (e.g. Fong & Geyer, 2001) potentially shown here by the less turbid waters on the south-facing coasts of Hinchinbrook Island.

Pattern C and Pattern D have a weaker dependance on CR discharge state as they are less turbid at the river mouth than B and have bimodal image date distributions with peaks outside of the June-Aug. period (Fig. 8 b). Pattern C shows the effect of downwelling wind (Fig. 11 b) wherein we infer sediments (either from resuspension or directly from the CR) are constrained to the coast by Ekman dynamics. Onshore Ekman transport can increase the baroclinic transport (Moffat & Lentz, 2012; Rennie et al., 1999) of the ACC and appears to be associated with high sediment loads that extend southwest past the tip of Kayak Island. Pattern D associates with relatively calm wind conditions, which may combine with lower sediment loads passing by the tip of Kayak Island; waters appear less turbid because less sediment is presumably mixed into the water column.

A subset of images filtered to remove those obtained during low CR discharge rates (Fig. 12) better shows the influence of wind across synoptic timescales. Pattern E (exemplified by Fig. 9 a) had the highest mean upwelling-favorable wind velocity and shows a response consistent with upwelling. The upshelf plume extension under upwelling is similar to the Columbia River plume's response to prevailing upwelling-favorable winds in summer, which cause the Columbia River plume to extend southwestward (García Berdeal, 2002; Hickey, 1989; Hickey et al., 1998). During such conditions, the Columbia River plume travels against its rotational tendency, and remains detached from the coast (Hickey et al., 2005). Pattern E shows a similar pattern although Kayak Island complicates the interpretation. Pattern F is associated with the lowest river discharge of the resolved SOM patterns. In this case, weakly downwelling-favorable winds combine with the Coriolis force to constrain the discharge to the western coast, leaving less turbid waters at the river mouth.

Pattern G associates with strong river discharge and the second highest mean upwelling-favorable wind velocity. The associated turbid water across the study region suggests the plume is spreading offshore or is in a transitory state of adjustment between a downshelf-directed plume and an upshelf-directed plume. Previous studies of such transitions in other ROFI systems (Hickey et al., 2005; Kourafalou et al., 1996; Zhou et al., 2023) indicate that this state is likely short-lived; we find it accounts for only a modest proportion of the clear sky images (FO = 14.3 %). Pattern H is similar to the 15 July 2020 satellite image (Fig. 9 b) and suggests that during high discharge and calm wind conditions, the distribution of sediments follows the expected turning imparted by the Coriolis force.

Offshore-directed plume water, potentially rich in silicic acid and iron (Ortega et al. in review), can be mapped using drifter trajectories and the high-discharge subset of SOM patterns. Offshore-directed flow from the CR region is most likely to occur in associated patterns E and G, which together comprise 37.5 % of the images in the subset. However, we expect the shelf break currents to inhibit continued offshore flow. The Kayak Island gyre appears to be a fairly permanent feature (Galt, 1976; Royer et al., 1979), and it alters cross-shelf transport, but drifter trajectories and SOM analyses indicate that surface waters originating at the plume are still capable of reaching and extending beyond the shelf break. CR plume suspended sediments are least likely to reach the shelf break in associated patterns F and H (62.5 % of the images in the subset), which are linked to weakly downwelling or calm wind conditions.

Data from the surface drifters deployed on the Middleton Line in July 2019 provide another perspective on the response of surface waters to alongshore winds and currents. Surface waters in the CR region entrained by the Kayak gyre were responsive to upwelling-favorable winds, as indicated by the two drifters that crossed the shelf break. Downwelling-favorable winds subsequently constrained some drifters to the coast (in a matter of days) as they simultaneously moved downshelf, and once past Hinchinbrook Island, surviving drifters diverted into PWS or continued downshelf past Montague Island, similar to model results by Wang et al. (2014). The cross shelf extent of the drifter tracks was comparable to model CR plume trajectories (Wang et al. 2014) under upwelling- and downwelling-favorable winds. The longest surviving drifters experienced similar magnitude upwelling-favorable winds near PWS, as occurred at the start of the deployment, yet did not advect far offshore, suggesting the reformation and persistence of the ACC near this location as indicated by Stabeno et al. (2016).

On a synoptic time scale, we found that increasingly negative alongshore wind (downwelling-favorable) is associated with increased downshelf transport in the upper 15 m (Fig. 15). An upwelling-favorable wind of 2.0 m/s is the weakest upwelling-favorable wind found to be associated with upshelf directed transport and qualitatively agrees with our interpretation of the SOM analysis. Our determined wind-current response time of 12 h matches the 12 h lag found in the first mode of Hickey et al.'s (1998) EOF analysis of regional wind-forced along-shelf currents near the Columbia River, but is double the 3–6 h response time the same study found for wind-forced plume current velocities. Comparing the July 2020 CR plume to the Jan. 1991 Columbia River plume at equal along-shelf distances (30 km) from their respective river mouths, the mean vertical practical salinity (S_P) gradient of the CR plume (1–12 km from MID 1 in Fig. 17) is 3.0 m^{-1} with σ of 0.82 versus the Columbia River plume's maximum vertical S_P gradient of 1 m^{-1} during similar downshelf-oriented plume directions. The Columbia River plume is also wider and deeper in calm wind conditions than the CR plume given the Columbia River's higher annual average discharge (Hickey et al., 1998; Thomas & Weatherbee, 2006). Relative to the CR plume, less buoyant, wider, and deeper plumes, such as the Columbia River plume (Hickey et al., 1998) are predicted to be less susceptible to wind stresses (Whitney & Garvine, 2005). Our results indicate that the true response time of CR plume's baroclinic transport to wind forcing was not captured in our analysis. A stationary CTD or current timeseries is likely necessary to resolve the response of the plume transport to wind forcing due to the short timescale of the spatiotemporal processes involved (e.g. internal tides or wind forcing) (Horner-Devine et al., 2015).

The Wang et al. (2014) study and our investigation of the Copper River plume both conclude that downwelling-plumes are typical during the month of July and that the plume spreads and thins in the offshore direction during upwelling-favorable winds. Both conclude that some small but likely non-negligible proportion of the riverine waters can escape the shelf system and directly interact with the HNLC basin waters. Our SOM patterns E and F (Fig. 12) approximately match the June-July Wang et al. (2014) locations of CR plume tracer during 2010 and 2011 (Fig. 7 a,b of Wang et al., 2014), which respectively experienced similar wind forcing as the SOM patterns E (upwelling-favorable winds) and H (downwelling-favorable winds). However, the proposed drivers of offshore transport are different between the two studies. In Wang et al. (2014) the offshore transport across the 200 m isobath is partly related to the build-up of plume water throughout August and a resulting frontal instability. Wind stress was shown to be uncorrelated to offshore transport across the 200 m isobath in Wang et al. (2014). In contrast, we show *in situ* evidence (Fig. 16) that surface waters near the CR mouth can pass the 200 m isobath in July, though such upwelling-favorable

conditions are uncommon and the discharge during our process study was approximately 50 % higher than July 2011. As freshwater in the mid-shelf region accumulates in July (Fig. 17 b), the potential for frontal instabilities to cross over the 200 m isobath increases but these were not observed in our study. While the Wang et al. (2014) study is somewhat limited by available observations, the high resolution hydrography, drifter tracks, and SOM analyses introduced herein provide new perspectives on the functioning of the Copper River plume. SOM analysis applied to hindcast numerical model integration results could usefully form the basis for a study that explicitly links modeled river-origin water with the turbid satellite-observed sediment plume patterns.

4.3. The role of the Copper River plume

During the 2019 and 2020 process studies the CR plume responded differently to contrasting wind stress conditions, which in turn affected stratification in the CR region. The sustained upwelling-favorable winds of 2019 dispersed the river plume offshore (see Fong and Geyer, 2001) (Fig. 17) before the river plume settled into an upshelf-oriented position that matched descriptions of Kourafalou et al. (1996) and circulated anti-cyclonically in the Kayak Island gyre. The Kayak Island gyre likely often encroaches on the Middleton Line, complicating the interpretation of data collected here (Fig. 9); however all the drifters deployed on July 4, 2019 had an eastward drift for at least 2 days indicating that the low (< 29) salinities (Fig. 17a) in the July 4, 2019 transect were partly a result of the CR plume remnants extending across the shelf, rather than recirculated water from the gyre.

Despite differences in discharge between the 4 July 2019 and 11 July 2020 Acrobat transects of the Middleton Line (Fig. 2; Fig. 17), the change in isohalines between the two transects indicates that the plume is sensitive to the upwelling (2019) and downwelling (2020) conditions. Downwelling tends to cause the foot of the plume to extend to a deeper isobath as the oceanic-plume front moves closer to shore (Lentz & Largier, 2006; Moffat & Lentz, 2012) while upwelling conditions enforce the opposite response (Lentz, 2004). During the 11 July 2020 transect the 29 isohaline extended from a depth of 11 m to 7 m with a mean slope of 7 $x10^{-4}$ between 6–16 km offshore from MID1, while on July 4, 2019 the 29 isohaline was flat at a depth of 5 m over the same distance and had several pools of low salinity water farther seaward.

Based on our understanding of plume response to wind forcing, and MODIS imagery from mid-June 2019 (NASA Worldview, 2012), in the following analysis we assume the plume state prior to the start of persistent upwelling-favorable winds on 20 June 2019 was similar to that of the 11 July 2020 transect. Assessing the potential influence of the upwelling conditions from the formulation of Lentz (2004), our estimates of adjusted plume width (27 km) and density anomaly (2.5 kg/m^3) are relatively close to our observations of 27–47 km and 3.5 kg/m^3, while the final plume thickness estimate (12 m) are more than twice the observed thickness (5 m). The divergent responses of theoretical and observed plume thickness may be a result of the survey's spatial and temporal limitations. The 25 July 2019 transect, which also experienced an upwelling wind stress prior to the observations, better shows an increase in plume thickness (at 23 km from shore) (Fig. 17 b). Our data are insufficient to address additional time-varying factors of the salinity field that relate to the Kayak Island gyre, the proximity of the measurements to the river mouth, or the delta type inflow of the river, but these topics would be worth targeting in future studies.

Silicic acid and salinity are used as tracers for assessing predictions by Eq. 5 relative to the observed values in the upwelling state and show upwelling-favorable wind can modify plume chemical characteristics. The 4 July 2019 observed concentrations averaged across MID2-MID4 for silicic acid were 9.5 μM ± 1.6 in the upper 10 m, considerably lower than the final predicted concentrations of 14.4–14.5 μM. The MID2-MID4 observed salinities within the plume boundary were 28.2 ± 0.6, higher than the predicted range of 25.7–26.0. Recalling that the initial values obtained from the mean of the upper 10 m of the plume were 19.6 μM SiO_4 and a salinity of 23.5, the predicted change in silicic acid and salinity accounted for 50 % and 55 % of the observed changes in concentration and salinity respectively, indicating the importance of upwelling-favorable winds in entraining subsurface water as a third mixing water end-member. Entrainment of subsurface water with higher salinity and lower silicic acid concentration relative to river water helps explain the observed water chemical characteristics. Additionally, any uptake of silicic acid by diatom production within plume waters (Strom, pers. comm.) would further reduce silicic acid concentrations. This simple model doesn't fully account for observed changes given the sampling limitations and the possibility that the actual entrained area in this region is greater than that predicted by Eq. 4, due to additional sources of entrainment mixing energy such as tides and waves (Horner-Devine et al., 2015); however, the concentration change is in the expected direction (i.e., higher salinity, lower silicic acid). These bulk averages also do not address further complexities such as the variability of light levels within the plume (Lohrenz et al., 1999) or the entrainment and advection of micronutrients (Ortega et al. in review) which can limit or enhance diatom production in the plume. These results help bound the degree to which upwelling-favorable winds establish bulk characteristics of the plume by modifying, for example, silicic acid concentrations and salinity.

4.4. Summary

While the Alaska Coastal Current (ACC) is primarily an along-shelf advective corridor of fresh coastal waters and geochemical tracers, it is also a leaky conduit that can feed low salinity cross-shelf eddy fluxes (Weingartner et al., 2005) or be interrupted by wind or topographically steered redirections (Stabeno et al., 2016). In addition to the ACC, we find that freshwater pathways recur in the mid-shelf region and at the shelf break, as evidenced by observations of low salinities at key spots along the ~ 250 km length of the Seward Line, which extends from the coast to the NGA basin. Summer discharge from the CR and the summer/fall along-slope diversion of low salinity ACC water by Kayak Island (located nearshore) appear to alter the salinity distributions near the Middleton Line and along the shelf break, particularly near Middleton Island. A narrow westward baroclinic current develops on the inner shelf in summer and fall while a broad westward baroclinic current builds during the same period across the mid to outer shelf. We suggest that tidal stirring and bathymetric steering at a shelf break canyon near Middleton Island also locally reduce salinities here.

Summer winds modify the Middleton Island transect hydrography as downwelling- and upwelling-favorable conditions drive salinity and suspended sediment distributions. Plume surface sediment patterns, a proxy for freshwater distribution, covary with river discharge and wind forcings. Elevated river discharge and upwelling-favorable winds in summer increase sediment loads just offshore of the CR river mouth, while downwelling-favorable winds typical of spring and fall drive the CR plume and sediment along the south-facing coasts of Hinchinbrook and Kayak islands. River discharge rates are predictably related to the variability in sediment at the river mouth. Satellite-tracked drifters and satellite images show that the CR plume is sensitive to Ekman dynamics. Hydrographic data from west of the river mouth show the ACC westward baroclinic transport of plume waters, while to the east of the river mouth an eastward baroclinic transport feeds a recurrent gyre that is located northwest of Kayak Island. The coastal baroclinic transport exhibits a significant relationship with alongshore wind velocities.

Process study cruises documented contrasting conditions, including a plume spreading event, so we applied theory (Lentz, 2004) to explore effects of wind stress on salinity, stratification, and silicic acid distributions within 50 km of the CR mouth. We found good agreement between theoretical predictions and observations for plume density anomalies and plume width, and while plume thickness was not well reproduced, the 4 July 2019 transect included some aspects beyond the scope of the theory. Caveats notwithstanding, we found that relative to

observations, predicted tracer concentrations within the modified plume were low in salinity and high in silicic acid. Additional processes beyond those in a simple upwelling-favorable wind analysis are needed to explain the 2019 Copper River plume salinity and silicic acid concentrations, though upwelling-favorable winds could account for half of the salinity and silicic acid signals.

Our assessment of freshwater pathways in the NGA reveals mid-shelf and shelf-break low salinities that impact stratification, currents and the fate of freshwater across this broad region. With perspectives across multiple length scales and seasons, our analysis of the Copper River plume helps explain how coastal water can efficiently spread to the shelf-break and beyond. These results carry implications for the ecological functioning of the NGA shelf ecosystem and production in the high-nutrient, low-chlorophyll waters of the adjacent slope and basin.

Funding

These data would not be possible without funding from the NSF's Northern Gulf of Alaska Long Term Ecological Research Program [OCE-1656070], the Exxon Valdez Oil Spill Trustee Council via the Gulf Watch Alaska program [21120114], and the North Pacific Research Board [L37].

CRediT authorship contribution statement

Isaac Reister: Writing – original draft, Writing – review & editing, Visualization, Formal analysis, Conceptualization, Investigation, Data curation, Methodology. **Seth Danielson:** Writing – review & editing, Supervision, Project administration, Methodology, Investigation, Funding acquisition, Data curation, Conceptualization. **Ana Aguilar-Islas:** Writing – review & editing, Resources, Project administration, Investigation, Funding acquisition, Data curation.

Declaration of competing interest

The authors declare that they have no known competing financial interests or personal relationships that could have appeared to influence the work reported in this paper.

Acknowledgements

We are indebted to the officers, crews, and marine technicians of the *R/V Nanuq*, *R/V Sikuliaq*, *R/V Tiglax*, whose assistance and expertise led to the data used herein. We thank Tyler Hennon, Suzanne Strom and Russ Hopcroft for useful discussions and edits as well as Mette Kaufman for nutrient analysis, Hank Statscewich and Kim Martini for Acrobat data processing, and Liz Dobbins for CTD data processing. We acknowledge the use of satellite imagery from the NASA Worldview application (https://worldview.earthdata.nasa.gov/), part of the NASA Earth Observing System Data and Information System (EOSDIS).

Appendix A. Supplementary material

Supplementary data to this article can be found online at https://doi.org/10.1016/j.pocean.2024.103373.

Data availability

Data will be made available on request.

References

Aguilar-Islas, A.M., Séguret, M.J.M., Rember, R., Buck, K.N., Proctor, P., Mordy, C.W., Kachel, N.B., 2016. Temporal variability of reactive iron over the Gulf of Alaska shelf. Deep Sea Res. Part II 132, 90–106. https://doi.org/10.1016/j.dsr2.2015.05.004.

Ahlnäs, K., Royer, T.C., George, T.H., 1987. Multiple dipole eddies in the Alaska Coastal Current detected with Landsat thematic mapper data. J. Geophys. Res. 92 (C12), 13041. https://doi.org/10.1029/JC092iC12p13041.

Beamer, J.P., Hill, D.F., Arendt, A., Liston, G.E., 2016. High-resolution modeling of coastal freshwater discharge and glacier mass balance in the Gulf of Alaska watershed. Water Resour. Res. 52 (5), 3888–3909. https://doi.org/10.1002/2015WR018457.

Brabets, T. P. (with Alaska). (1997). *Geomorphology of the lower Copper River, Alaska*. U.S. Geological Survey Professional Paper 1581.

Brown, M.T., Lippiatt, S.M., Bruland, K.W., 2010. Dissolved aluminum, particulate aluminum, and silicic acid in northern Gulf of Alaska coastal waters: Glacial/riverine inputs and extreme reactivity. Mar. Chem. 122 (1–4), 160–175. https://doi.org/10.1016/j.marchem.2010.04.002.

Carmack, E.C., 2007. The alpha/beta ocean distinction: a perspective on freshwater fluxes, convection, nutrients and productivity in high-latitude seas. Deep Sea Res. Part II 54 (23–26), 2578–2598. https://doi.org/10.1016/j.dsr2.2007.08.018.

Chen, J.L., Wilson, C.R., Tapley, B.D., 2006. Satellite gravity measurements confirm accelerated melting of Greenland ice sheet. Science (New York, N.Y.) 313 (5795), 1958–1960. https://doi.org/10.1126/science.1129007.

Choi, B.-J., Wilkin, J.L., 2007. The effect of wind on the dispersal of the Hudson River plume. J. Phys. Oceanogr. 37 (7), 1878–1897. https://doi.org/10.1175/JPO3081.1.

Danielson, S. L., Hedstrom, K. S., & Curchitser, E. (2016). *Cook Inlet Circulation Model Calculations, Final Report to Bureau of Ocean Energy Management* (Final Report M14AC00014; Bureau of Ocean Energy Managemetn Alaska Environmental Studies Program, p. 149). University of Alaska Fairbanks. https://www.boem.gov/sites/default/files/uploadedFiles/BOEM/BOEM_Newsroom/Library/Publications/BOEM_2015-050_LoRes.pdf.

Danielson, S.L., Hill, D.F., Hedstrom, K.S., Beamer, J., Curchitser, E., 2020. Demonstrating a high-resolution Gulf of Alaska ocean circulation model forced across the coastal interface by high-resolution terrestrial hydrological models. J. Geophys. Res. Oceans 125 (8). https://doi.org/10.1029/2019JC015724.

De Boer, G.J., Pietrzak, J.D., Winterwerp, J.C., 2009. SST observations of upwelling induced by tidal straining in the Rhine ROFI. Cont. Shelf Res. 29 (1), 263–277. https://doi.org/10.1016/j.csr.2007.06.011.

Dodimead, A.J., Favorite, F., Hirano, T., 1963. Review of oceanography of the Subarctic Pacific region. International North Pacific Fisheries Commission Bulletin 13, 1–195.

Earth Science Data Systems, N. (2023). *Earthdata*. Earthdata; Earth Science Data Systems, NASA. https://www.earthdata.nasa.gov/homepage.

Ekman, V.W., 1905. On the influence of the earth's rotation on ocean-currents. Ark. Mat. Astr. Fys. 2 (11), 1–52.

Fang, Y., Potter, R.A., Statscewich, H., Weingartner, T.J., Winsor, P., Irving, B.K., 2017. Surface current patterns in the northeastern Chukchi Sea and their response to wind forcing. J. Geophys. Res. Oceans 122 (12), 9530–9547. https://doi.org/10.1002/2017JC013121.

Feely, R.A., Baker, E.T., Schumacher, J.D., Massoth, G.J., Landing, W.M., 1979. Processes affecting the distribution and transport of suspended matter in the northeast Gulf of Alaska. Deep Sea Res. Part A 26 (4), 445–464. https://doi.org/10.1016/0198-0149(79)90057-8.

Firing, E., Hummon, J., Chereskin, T., 2012. Improving the quality and accessibility of current profile measurements in the Southern ocean. Oceanography 25 (3), 164–165. https://doi.org/10.5670/oceanog.2012.91.

Fong, D.A., Geyer, W.R., 2001. Response of a river plume during an upwelling favorable wind event. J. Geophys. Res. Oceans 106 (C1), 1067–1084. https://doi.org/10.1029/2000JC900134.

Galt, J.A., 1976. Circulation studies on the Alaskan continental shelf off the Copper River delta (NOAA Technical Report RU 81; p. 46). NOAA.

García Berdeal, I., 2002. Influence of wind stress and ambient flow on a high discharge river plume. J. Geophys. Res. 107 (C9), 3130. https://doi.org/10.1029/2001JC000932.

Greenland, S., Senn, S.J., Rothman, K.J., Carlin, J.B., Poole, C., Goodman, S.N., Altman, D.G., 2016. Statistical tests, P values, confidence intervals, and power: A guide to misinterpretations. Eur. J. Epidemiol. 31 (4), 337–350. https://doi.org/10.1007/s10654-016-0149-3.

Harrison, P., Clifford, P., Cochlan, W., Yin, K., StJohn, M., Thompson, P., Sibbald, M., Albright, L., 1991. Nutrient and plankton dynamics in the Fraser River plume, Strait of Georgia, British Columbia. Mar. Ecol. Prog. Ser. 70, 291–304. https://doi.org/10.3354/meps070291.

Helland-Hansen, B., 1934. The Sognefjord section—Oceanographic observations in the northernmost part of the North Sea and the southern part of the Norwegian Sea. Lancashire Sea-Fish. Lab, James Johnstone Memorial Volume.

Hersbach, H., Bell, B., Berrisford, P., Hirahara, S., Horányi, A., Muñoz-Sabater, J., Nicolas, J., Peubey, C., Radu, R., Schepers, D., Simmons, A., Soci, C., Abdalla, S., Abellan, X., Balsamo, G., Bechtold, P., Biavati, G., Bidlot, J., Bonavita, M., Thépaut, J., 2020. The ERA5 global reanalysis. Q. J. R. Meteorolog. Soc. 146 (730), 1999–2049. https://doi.org/10.1002/qj.3803.

Hickey, B.M., Pietrafesa, L.J., Jay, D.A., Boicourt, W.C., 1998. The Columbia River plume study: Subtidal variability in the velocity and salinity fields. J. Geophys. Res. Oceans 103 (C5), 10339–10368. https://doi.org/10.1029/97JC03290.

Hickey, B.M., Geier, S., Kachel, N., MacFadyen, A., 2005. A bi-directional river plume: the Columbia in summer. Cont. Shelf Res. 25 (14), 1631–1656. https://doi.org/10.1016/j.csr.2005.04.010.

Hickey, B.M., 1989. Chapter 2 patterns and processes of circulation over the Washington continental shelf and slope. In: Landry, M.R., Hickey, B.M. (Eds.), Coastal Oceanography of Washington and Oregon, Vol. 47, pp. 41–115. https://doi.org/10.1016/S0422-9894(08)70346-5.

Hill, D.F., Bruhis, N., Calos, S.E., Arendt, A., Beamer, J., 2015. Spatial and temporal variability of freshwater discharge into the Gulf of Alaska. J. Geophys. Res. Oceans 120 (2), 634–646. https://doi.org/10.1002/2014JC010395.

Himes-Cornell, A., Kasperski, S., 2016. Using socioeconomic and fisheries involvement indices to understand Alaska fishing community well-being. Coast. Manag. 44 (1), 36–70. https://doi.org/10.1080/08920753.2016.1116671.
Holling, C.S., 1973. Resilience and stability of ecological systems. Annual Review of Ecology and Ssstematics 4, 1–23.
Hopcroft, R. R., Aguilar-Islas, A. M., Danielson, S. L., Fiechter, J., Strom, S.L., 2016. LTER: Resilience in the environmental mosaic of the Northern Gulf of Alaska (NGA) shelf ecosystem. https://nga.lternet.edu/wp-content/uploads/2018/06/LTER-FastLane.FINAL-short.pdf.
Horner-Devine, A.R., Hetland, R.D., MacDonald, D.G., 2015. Mixing and transport in coastal river plumes. Annu. Rev. Fluid Mech. 47 (1), 569–594. https://doi.org/10.1146/annurev-fluid-010313-141408.
Houghton, R.W., Tilburg, C.E., Garvine, R.W., Fong, A., 2004. Delaware River plume response to a strong upwelling-favorable wind event. Geophys. Res. Lett. 31 (7), L07302. https://doi.org/10.1029/2003GL018988.
Jaeger, J.M., Nittrouer, C.A., Scott, N.D., Milliman, J.D., 1998. Sediment accumulation along a glacially impacted mountainous coastline: North-east Gulf of Alaska. Basin Res. 10 (1), 155–173. https://doi.org/10.1046/j.1365-2117.1998.00059.x.
Johnson, G.C., Toole, J.M., Larson, N.G., 2007. Sensor corrections for Sea-Bird SBE-41CP and SBE-41 CTDs. J. Atmos. Oceanic Tech. 24 (6), 1117–1130. https://doi.org/10.1175/JTECH2016.1.
Klinger, B.A., 1994. Inviscid current separation from rounded capes. J. Phys. Oceanogr. 24 (8), 1805–1811. https://doi.org/10.1175/1520-0485(1994)024<1805:ICSFRC>2.0.CO;2.
Kohonen, T., 1982. Self-organized formation of topologically correct feature maps. Biol. Cybern. 43 (1), 59–69. https://doi.org/10.1007/BF00337288.
Kourafalou, V.H., Oey, L.-Y., Wang, J.D., Lee, T.N., 1996. The fate of river discharge on the continental shelf: 1. Modeling the river plume and the inner shelf coastal current. J. Geophys. Res. Oceans 101 (C2), 3415–3434. https://doi.org/10.1029/95JC03024.
Ladd, C., Cheng, W., Salo, S., 2016. Gap winds and their effects on regional oceanography Part II: Kodiak Island, Alaska. Deep Sea Res. Part II 132, 54–67. https://doi.org/10.1016/j.dsr2.2015.08.005.
Large, W.G., Pond, S., 1981. Open ocean momentum flux measurements in moderate to strong winds. J. Phys. Oceanogr. 11 (3), 324–336. https://doi.org/10.1175/1520-0485(1981)011<0324:OOMFMI>2.0.CO;2.
Lentz, S.J., 2004. The response of buoyant coastal plumes to upwelling-favorable winds*. J. Phys. Oceanogr. 34 (11), 2458–2469. https://doi.org/10.1175/JPO2647.1.
Lentz, S.J., Largier, J., 2006. The influence of wind forcing on the Chesapeake Bay buoyant coastal current*. J. Phys. Oceanogr. 36 (7), 1305–1316. https://doi.org/10.1175/JPO2909.1.
Levin, S.A., Lubchenco, J., 2008. Resilience, robustness, and marine ecosystem-based management. Bioscience 58 (1), 27–32. https://doi.org/10.1641/B580107.
Liu, Y., 2005. Patterns of ocean current variability on the West Florida shelf using the self-organizing map. J. Geophys. Res. 110 (C6), C06003. https://doi.org/10.1029/2004JC002786.
Livingstone, D., Royer, T.C., 1980. Observed surface winds at Middleton Island, Gulf of Alaska and their influence on the ocean circulation. J. Phys. Oceanogr. 10 (5), 753–764. https://doi.org/10.1175/1520-0485(1980)010<0753:OSWAMI>2.0.CO;2.
Loescher, K.A., Young, G.S., Colle, B.A., Winstead, N.S., 2006. Climatology of barrier jets along the Alaskan coast. Part I: Spatial and temporal distributions. Mon. Weather Rev. 134 (2), 437–453. https://doi.org/10.1175/MWR3037.1.
Lohan, M.C., Bruland, K.W., 2006. Importance of vertical mixing for additional sources of nitrate and iron to surface waters of the Columbia River plume: Implications for biology. Mar. Chem. 98 (2–4), 260–273. https://doi.org/10.1016/j.marchem.2005.10.003.
Lohrenz, S.E., Fahnenstiel, G.L., Redalje, D.G., Lang, G.A., Dagg, M.J., Whitledge, T.E., Dortch, Q., 1999. Nutrients, irradiance, and mixing as factors regulating primary production in coastal waters impacted by the Mississippi River plume. Cont. Shelf Res. 19 (9), 1113–1141. https://doi.org/10.1016/S0278-4343(99)00012-6.
Loos, E.A., Costa, M., 2010. Inherent optical properties and optical mass classification of the waters of the Strait of Georgia, British Columbia, Canada. Progr. Oceanogr. 87 (1–4), 144–156. https://doi.org/10.1016/j.pocean.2010.09.004.
Macklin, S.A., Lackmann, G.M., Gray, J., 1988. Offshore-directed winds in the vicinity of Prince William Sound, Alaska. Monthly Weather Review 116 (6), 1289–1301. https://doi.org/10.1175/1520-0493(1988)116<1289:ODWITV>2.0.CO;2.
Martini, K., Statscewich, H., Danielson, S., Reister, I., 2023. isreister/ACROBAT: V1.0.0_UAFOceansACROBAT (Version v1.0.0UAF_ACROBAT) [Computer software]. Zenodo. https://doi.org/10.5281/ZENODO.7768458.
McDowell Group, 2020. The economic value of Alaska's seafood industry. Alaska Seafood Marketing Institute. https://uploads.alaskaseafood.org/2020/01/McDowell-Group_ASMI-Economic-Impacts-Report-JAN-2020.pdf.
Mesquita, M.S., Atkinson, D.E., Hodges, K.I., 2010. Characteristics and variability of storm tracks in the North Pacific, Bering Sea, and Alaska*. J. Clim. 23 (2), 294–311. https://doi.org/10.1175/2009JCLI3019.1.
MODIS Science Team, 2017. MOD02QKM MODIS/Terra Calibrated Radiances 5-Min L1B Swath 250m [Dataset]. NASA Level 1 and Atmosphere Archive and Distribution System Distributed Active Archive Center. https://doi.org/10.5067/MODIS/MOD02QKM.061.
Moffat, C., Lentz, S.J., 2012. On the response of a buoyant plume to downwelling-favorable wind stress. J. Phys. Oceanogr. 42 (7), 1083–1098. https://doi.org/10.1175/JPO-D-11-015.1.
Mordy, C.W., Stabeno, P.J., Kachel, N.B., Kachel, D., Ladd, C., Zimmermann, M., Hermann, A.J., Coyle, K.O., Doyle, M.J., 2019. Patterns of flow in the canyons of the northern Gulf of Alaska. Deep Sea Res. Part II 165, 203–220. https://doi.org/10.1016/j.dsr2.2019.03.009.
Musgrave, D.L., Weingartner, T.J., Royer, T.C., 1992. Circulation and hydrography in the northwestern Gulf of Alaska. Deep Sea Res. Part A 39 (9), 1499–1519. https://doi.org/10.1016/0198-0149(92)90044-T.
Narayanan, C., Garvine, R.W., 2002. Formation of a shelfbreak front by freshwater discharge. Dyn. Atmos. Oceans 36 (1–3), 103–124. https://doi.org/10.1016/S0377-0265(02)00027-1.
NASA Worldview, 2012. NASA Worldview. Earth Observing System Data and Information System (EOSDIS). https://www.earthdata.nasa.gov/worldview.
Neal, E.G., Hood, E., Smikrud, K., 2010. Contribution of glacier runoff to freshwater discharge into the Gulf of Alaska: GULF OF ALASKA GLACIER RUNOFF. Geophys. Res. Lett. 37 (6), n/a-n/a. https://doi.org/10.1029/2010GL042385.
NOAA, 2024. Hinchinbrook Cape Home Page—NOAA Tides & Currents. https://tidesandcurrents.noaa.gov/stationhome.html?id=9454329#sensors.
Pawlowicz, R., Di Costanzo, R., Halverson, M., Devred, E., Johannessen, S., 2017. Advection, surface area, and sediment load of the Fraser River plume under variable wind and river forcing. Atmos. Ocean 55 (4–5), 293–313. https://doi.org/10.1080/07055900.2017.1389689.
Powers, S.P., Bishop, M.A., Grabowski, J.H., Peterson, C.H., 2002. Intertidal benthic resources of the Copper River delta, Alaska, USA. J. Sea Res. 47 (1), 13–23. https://doi.org/10.1016/S1385-1101(01)00102-2.
Rennie, S.E., Largier, J.L., Lentz, S.J., 1999. Observations of a pulsed buoyancy current downstream of Chesapeake Bay. J. Geophys. Res. Oceans 104 (C8), 18227–18240. https://doi.org/10.1029/1999JC900153.
Rodionov, S.N., Bond, N.A., Overland, J.E., 2007. The Aleutian Low, storm tracks, and winter climate variability in the Bering Sea. Deep Sea Res. Part II 54 (23–26), 2560–2577. https://doi.org/10.1016/j.dsr2.2007.08.002.
Royer, T.C., 1982. Coastal fresh water discharge in the northeast Pacific. J. Geophys. Res. 87 (C3), 2017. https://doi.org/10.1029/JC087iC03p02017.
Royer, T.C., 2005. Hydrographic responses at a coastal site in the northern Gulf of Alaska to seasonal and interannual forcing. Deep Sea Res. Part II 52 (1–2), 267–288. https://doi.org/10.1016/j.dsr2.2004.09.022.
Royer, T.C., Hansen, D.V., Pashinski, D.J., 1979. Coastal flow in the northern Gulf of Alaska as observed by dynamic topography and satellite-tracked drogued drift buoys. J. Phys. Oceanogr. 9 (4), 785–801. https://doi.org/10.1175/1520-0485(1979)009<0785:CFITNG>2.0.CO;2.
Salisbury, J., Campbell, J., Linder, E., Davidmeeker, L., Mullerkarger, F., Vorosmarty, C., 2004. On the seasonal correlation of surface particle fields with wind stress and Mississippi discharge in the northern Gulf of Mexico. Deep Sea Res. Part II 51 (10–11), 1187–1203. https://doi.org/10.1016/S0967-0645(04)00107-9.
Sandy, S.J., Danielson, S.L., Mahoney, A.R., 2022. Automating the acoustic detection and characterization of sea ice and surface waves. J. Mar. Sci. Eng. 10 (11), 1577. https://doi.org/10.3390/jmse10111577.
Sea-Bird Scientific. (2017). *SBE Data Processing* [C++; Windows PC]. Sea-Bird Scientific. https://www.seabird.com/software.
Stabeno, P.J., Bond, N.A., Hermann, A.J., Kachel, N.B., Mordy, C.W., Overland, J.E., 2004. Meteorology and oceanography of the northern Gulf of Alaska. Cont. Shelf Res. 24 (7–8), 859–897. https://doi.org/10.1016/j.csr.2004.02.007.
Stabeno, P.J., Bell, S., Cheng, W., Danielson, S., Kachel, N.B., Mordy, C.W., 2016. Long-term observations of Alaska Coastal Current in the northern Gulf of Alaska. Deep Sea Res. Part II 132, 24–40. https://doi.org/10.1016/j.dsr2.2015.12.016.
Strom, S.L., Olson, M.B., Macri, E.L., Mord, C.W., 2006. Cross-shelf gradients in phytoplankton community structure, nutrient utilization, and growth rate in the coastal Gulf of Alaska. Mar. Ecol. Prog. Ser. 328, 75–92. https://doi.org/10.3354/meps328075.
Sumaila, U.R., Cheung, W.W.L., Lam, V.W.Y., Pauly, D., Herrick, S., 2011. Climate change impacts on the biophysics and economics of world fisheries. Nat. Clim. Chang. 1 (9), 449–456. https://doi.org/10.1038/nclimate1301.
Tennant, W., 2004. Considerations when using pre-1979 NCEP/NCAR reanalyses in the southern hemisphere. Geophys. Res. Lett. 31 (11). https://doi.org/10.1029/2004GL019751.
Thomas, A., Weatherbee, R., 2006. Satellite-measured temporal variability of the Columbia River plume. Remote Sens. Environ. 100 (2), 167–178. https://doi.org/10.1016/j.rse.2005.10.018.
Thomson, R. E., & Emery, W. J., 2014a. Chapter 5—Time series analysis methods. In R. E. Thomson & W. J. Emery (Eds.), Data Analysis Methods in Physical Oceanography (Third Edition) (Third Edition, pp. 425–591). Elsevier. https://doi.org/10.1016/B978-0-12-387782-6.00005-3.
Thomson, R.E., Emery, W.J., 2014b. Statistical methods and error handling. In Data Analysis Methods in Physical Oceanography (pp. 219–311). Elsevier. https://doi.org/10.1016/B978-0-12-387782-6.00003-X.
Thomson, R.E., Emery, W.J., 2014c. The spatial analyses of data fields. In Data Analysis Methods in Physical Oceanography (pp. 313–424). Elsevier. https://doi.org/10.1016/B978-0-12-387782-6.00004-1.
Verspecht, F., Rippeth, T.P., Howarth, M.J., Souza, A.J., Simpson, J.H., Burchard, H., 2009. Processes impacting on stratification in a region of freshwater influence: application to Liverpool Bay, 2009JC005475 J. Geophys. Res. Oceans 114 (C11). https://doi.org/10.1029/2009JC005475.
Vesanto, J., Alhoniemi, E., Himberg, J., Kiviluoto, K., Parviainen, 1999. Self-organizing map for data mining in MATLAB: the SOM toolbox. Simulation News Europe, 25, 54.
Walker, N.D., 1996. Satellite assessment of Mississippi River plume variability: causes and predictability. Remote Sens. Environ. 58 (1), 21–35. https://doi.org/10.1016/0034-4257(95)00259-6.
Walker, N.D., Wiseman, W.J., Rouse, L.J., Babin, A., 2005. Effects of river discharge, wind stress, and slope eddies on circulation and the satellite-observed structure of

the Mississippi River plume. J. Coast. Res. 216, 1228–1244. https://doi.org/10.2112/04-0347.1.
Wang, J., 2004. A hydrological digital elevation model for freshwater discharge into the Gulf of Alaska. J. Geophys. Res. 109 (C7), C07009. https://doi.org/10.1029/2002JC001430.
Wang, Y., Xue, H., Chai, F., Chao, Y., Farrara, J., 2014. A model study of the Copper River plume and its effects on the northern Gulf of Alaska. Ocean Dyn. 64 (2), 241–258. https://doi.org/10.1007/s10236-013-0684-3.
Weingartner, T.J., Danielson, S.L., Royer, T.C., 2005. Freshwater variability and predictability in the Alaska Coastal Current. Deep Sea Res. Part II 52 (1–2), 169–191. https://doi.org/10.1016/j.dsr2.2004.09.030.
Whitney, F.A., Crawford, W.R., Harrison, P.J., 2005. Physical processes that enhance nutrient transport and primary productivity in the coastal and open ocean of the subarctic NE Pacific. Deep Sea Res. Part II 52 (5–6), 681–706. https://doi.org/10.1016/j.dsr2.2004.12.023.
Whitney, M.M., Garvine, R.W., 2005. Wind influence on a coastal buoyant outflow. J. Geophys. Res. Oceans 110 (C3). https://doi.org/10.1029/2003JC002261.
Williams, W.J., Weingartner, T.J., Hermann, A.J., 2007. Idealized three-dimensional modeling of seasonal variation in the Alaska Coastal Current. J. Geophys. Res. 112 (C7), C07001. https://doi.org/10.1029/2005JC003285.
Zhou, J., Izett, J.G., Edwards, C.A., Damien, P., Kessouri, F., McWilliams, J.C., 2023. Modeling the dispersal of the San Francisco Bay plume over the northern and central California shelf. Estuar. Coast. Shelf Sci. 287, 108336. https://doi.org/10.1016/j.ecss.2023.108336.